TECHNISCHE UNIVERSITÄT WIEN

Diplomarbeit

Exceptional points in graphene nanoribbons

by

Tobias Reisch, BSc

Matrikelnummer 01128201
Mühlegasse 5
6820 Frastanz

Supervisor:

Assistant Prof. Dr. Florian Libisch

Institute Of Theoretical Physics
Vienna University of Technology

Vienna, 24.10.2018, _____

Zusammenfassung

Exceptional points (EPs, deutsch "außergewöhnliche Punkte") sind Singularitäten die im Eigenwertspektrum von nicht-hermitschen Operatoren auftreten. Sie kommen in einer Bandbreite von Systemen vor und liegen vielen – oftmals überraschenden – Phänomenen zugrunde. Solch ein Effekt ist die chirale Umwandlung von Zuständen, wenn externe Parameter adiabatisch und entlang eines zirkulären Pfades um einen EP im Parameterraum variiert werden. In diesem Beispiel hängt das Ergebnis davon ab, ob der Pfad im oder gegen den Uhrzeigersinn durchlaufen wird. In eine Richtung hält das adiabatische Theorem, in die andere bricht es zusammen.

In dieser Dipolmarbeit identifizieren wir EPs in Armchair und Zigzag Graphen Nanobändern und simulieren die Dynamik während sie umrundet werden. Wir finden EPs die generisch an den Rändern einer Bandlücke auftreten und eine Klasse EPs die sich nicht-generisch an echten Kreuzungen in der Bandstuktur von Armchairbändern bildet. Wir können zeigen, dass die dynamische Variation von Parametern um und in der Umgebung von generischen EPs nicht-hermitsche Effekte, aber keine chirale Zustandsumwandlung zur Folge hat. Um nicht-generische EPs hingengen finden wir chirale Zustandsumwandlung für eine Vielzahl an möglichen Parameterpfaden und Nanobandlängen. Wir runden die Arbeit mit einigen Gedanken zu eventuellen experimentellen Realisierungen ab.

Abstract

Exceptional points (EPs) are singularities in the spectrum of non-hermitian operators. They occur in a wide range of systems and lead to many – often counterintuitive – effects. One such effect is the chiral state conversion upon adiabatic, circular variation of external parameters around an EP. For one encircling direction the adiabatic theorem holds, whereas for the other direction it breaks down, resulting in a different outcome depending on the encircling direction.

In this thesis we identify exceptional points in armchair and zigzag graphene nanoribbons and, subsequently, simulate dynamically encircling them. We find EPs occurring generically at the edges of a bandgap and an EP emerging non-generically at real crossings in the bandstructure of armchair ribbons. We can show that dynamical parameter variations around and in the vicinity of generic EPs yield non-hermitian effects, but no chiral state conversion. We find, however, chiral state conversion when encircling non-generic EPs for a broad spectrum of parameter paths and ribbon lengths. In the end, we conclude with comments on potential realizations in experiment.

Contents

1 Introduction

Exceptional points appear in a wide range of systems. They are a phenomenon arising due to non-hermitian physics, which, in a nutshell, incorporate an effective description of not included degrees of freedom [1]. Depending on the system where the exceptional point (EP) can be found in, its physical interpretation can vary strongly [2]. However, they all have in common that at the EP two (or more) modes (or wavefunctions) coalesce, resulting in a defective Hilbert-space. We will elaborate on this in chapter 2. In the last twenty years researchers realized that EPs are not just mathematical peculiarities that present an obstacle for approximative schemes, but a significant physical phenomenon, that has been extensively studied in electrodynamics, mechanics, optics, atomic and molecular physics [2].

A recent experiment by Doppler et al. [3], in which our group was involved, presented the dynamical encircling of an exceptional point. In this experiment the boundary conditions of a microwave resonator were varied adiabatically, such that the parameter trajectory of the microwave would encircle an EP. Due to the particular structure of the eigenvalues, one naïvely expects one state to be converted into the other upon encircling the EP. However, due to the non-hermitian terms that give rise to the EP the adiabatic theorem [4] only holds for one initial state, while it breaks down for the other. Subsequently, dynamically encircling an exceptional point results in a different result when encircling clockwise or counterclockwise, creating an asymmetric switch. We will discuss this phenomenon in greater detail in chapter 2.

The idea of an asymmetric switch is intriguing, not only for microwave-guides, but for many other systems, such as graphene. Graphene is the first two-dimensional material that has been isolated and has gained a lot of attention since then [5]. It consists of a single layer of carbon atoms arranged in a hexagonal honeycomb lattice. Around the Fermi energy its bandstructure can be approximated very well by two cones at the two inequivalent corners of the Brillouin zone (compare with Fig. 3.2). Its exceptional bandstructure has two consequences which are partly responsible for its recent success. Firstly, the bandstructure around the Fermi energy is approximately linear, turning the electrons in graphene into a solid-state analogue of massless Dirac-fermions[1], often called Dirac quasiparticles. Secondly, the Dirac cones are strongly separated in momentum space, introducing an additional degree of freedom, the "valley".

The valley degree of freedom is notoriously hard to control, and a lot of research has been invested in this direction, working towards the long-term goal of "valleytronics"[6]. This diploma thesis was initiated in order to investigate the existence and effects of

---

[1]In contrast to the parabolic dispersion $E(k) = \frac{\hbar^2 k^2}{2m}$ usually observed in metals, a linear one resembles the relativistic energy-momentum relation for $m = 0$ $E = cp$.

exceptional points in graphene, perhaps enabling us to propose an asymmetric switch to control the valley degree of freedom[2].

In analogy to Doppler et al. [3] we will map the adiabatic variation of external parameters to a slow change of these external parameters along a graphene nanoribbon. Graphene nanoribbons are strips of graphene that extend in one direction much longer than in the other. Generally, we consider graphene nanoribbons with either armchair or zigzag edges (compare with Fig. 3.7) and we identify exceptional points in their electronic structure.

There is not much literature concerning exceptional point physics in graphene nanoribbons. One study by Fagotti et al. [8] shows the existence of EPs in armchair ribbons, associating them with the breakdown of parity-time ($\mathcal{PT}$-)symmetry. Their study relies on an approximation of the bandstructure similar to the Dirac equation and merely proves the existence of EPs in armchair nanoribbons. They conclude with the following remark:

> "An aspect that certainly deserves further study is the effect of exceptional points on the transport properties of graphene nanoribbons in the presence of a potential that varies also in the longitudinal direction. Moreover, it would be interesting to study more in depth the properties of complex eigenmodes [...]." – Fagotti et al. [8].

Although they did not follow up on these ideas, they foreshadowed this thesis. In particular we start this thesis by studying the behavior of the complex eigenmodes of the nanoribbons. Tracking the eigenvalues of two modes as a function of two (or more) external parameters results in the Riemann surface[3] of the two modes. Subsequently, this Riemann surface can be used to investigate the position of EPs and the topology of the Riemann surface itself. The topology itself is then necessary to understand the phenomena that occur when investigateing transport in longitudinally varying potentials.

Albeit there is not much literature on exceptional points in graphene nanoribbons, we can draw conclusions from similar systems. A lot of research concerning exceptional point physics has been conducted in optics. In $\mathcal{PT}$-symmetric hexagonal photonic lattices introducing a real mass for the Dirac-quasiparticles results in a bandgap opening at the Dirac-point, whereas introducing an imaginary mass seems to "push" the Dirac cones together [9], resulting in exactly the same behavior we will observe in chapter 3.2. In a similar way this behavior of a Dirac cone was realized experimentally by Zhen et al. using photonic crystals [10]: they identified the ring where the Dirac cones intersect with a ring of exceptional points.

We adapt the presented concepts to graphene nanoribbons and present the characteristics, limitations and potentials of exceptional points in graphene nanoribbons.

---

[2]Although the literature sometimes calls this phenomenon "topological switch", recent research [7] hints that this is not actually true, therefore we refrain from this expression.

[3]The notion Riemann surface is borrowed from complex mathematics due to the connection of the eigenvalue structure around the EP to the square root of a complex number.

2 Non-hermitian physics

2.1 Motivation

One of the pillars of our modern understanding of physics is energy conservation for a closed system. As a consequence, the standard formulation of quantum mechanics deals with hermitian Hamiltonians, exhibiting real eigenenergies and therefore unitary time evolution. However, very often we want to focus on the relevant physics in a small subsystem replacing the surrounding by an effective treatment. The resulting open quantum system features complex eigenenergies. George Gamov [11] was the first to show in a study on alpha decay that quantum states which have a probability to tunnel out of the nucleus can be effectively described by complex eigenvalues. The real and imaginary parts of the complex eigenvalues correspond to the experimentally found energy levels and widths of the nuclear resonances, respectively. This was the birth of non-hermitian quantum mechanics. It developed into a valuable tool, able to describe dissipative systems, helping to understand effects by focusing on the system of interest and simplifying the effect of the surroundings. Perhaps one of the most striking features of non-hermitian quantum mechanics are exceptional points, also known as branch-point singularities. At an exceptional point the eigenvalues "coalesce", but in contrast to a conventional degeneracy also the eigenvectors are exactly parallel. Exceptional points occur in many different systems, are associated with many interesting phenomena and are subject to a lot of current research [2, 12]. This chapter will give a brief introduction to exceptional points, highlighting all their features that are necessary to understand the effects discussed in this thesis.

2.2 Exceptional Points

In the following we will examine a simple non-hermitian Hamiltonian to demonstrate the emergence and basic properties of an exceptional point. Exceptional points (EPs) occur in general in systems with (infinitely) many eigenstates, but in the vicinity of an EP the full behavior of the two levels involved can be modeled by a 2×2-matrix. Even in systems with several EPs the effects observed are merely a combination of two-level EPs [13, 14][1]. To illustrate the properties of EPs we therefore restrict ourselves to a two level system. The following general remarks are based on [2, 7].

Consider the Hamiltonian

$$H = \begin{pmatrix} \omega_1 + i\frac{\gamma_1}{2} & g \\ g & \omega_2 + i\frac{\gamma_2}{2} \end{pmatrix} \qquad \omega_i, \gamma_i, g \in \mathbb{R}; \gamma > 0 \qquad (2.1)$$

It is not completely general, but it captures the most important effects of EPs which will be discussed later in this chapter.

In standard hermitian quantum mechanics the dual vector $\langle v|$ of a vector $|v\rangle$ is given by its hermitian conjugate $\langle v| = (|v\rangle)^\dagger$. Hence, the inner product is calculated via

$$\langle v|v\rangle \equiv (|v\rangle)^\dagger |v\rangle \ . \qquad (2.2)$$

For a Hamiltonian that is non-hermitian, $H^\dagger \neq H$, as in Eq. (2.1), the eigenvectors are not necessarily orthogonal with respect to the inner product defined in Eq. (2.2). In non-hermitian quantum mechanics we therefore independently consider right $H |v_i\rangle = \epsilon_i |v_i\rangle$ and left $\langle u_i^*| H = \tilde{\epsilon} \langle u_i^*|$ eigenvectors. The asterisk denotes the "dual basis" [2]. Because the $\langle u_i^*|$ were chosen as dual basis, there is an orthogonality relation $\langle u_i^*|v_j\rangle = \delta_{ij}$ as well as a closure relation $\sum_i |v_i\rangle \langle u_i^*| = \mathbb{I}$.

For simplicity, but without the loss of generality, we perform a gauge transformation of H:

$$\tilde{H} = \begin{pmatrix} -\omega - i\frac{\gamma}{2} & g \\ g & \omega + i\frac{\gamma}{2} \end{pmatrix} \quad \text{with} \quad \omega = \frac{\omega_2 - \omega_1}{2} \qquad \gamma = \frac{\gamma_1 - \gamma_2}{2}. \qquad (2.3)$$

The eigenvalues of $\tilde{H}$ are

$$\lambda_\pm = \pm\lambda = \pm\sqrt{(\omega + i\frac{\gamma}{2})^2 + g^2}. \qquad (2.4)$$

The argument of the square root in Eq. (2.4) is a complex number, hence, in order to understand $\lambda_\pm$ better, it is instructive to examine the properties of the complex square root function. Let us start with a complex number in polar representation $z = re^{i\phi}, \phi \in (-\pi, \pi]$ (red arrow in Fig. 2.1). Because the square root is multivalued, we

---

[1]There are higher order EPs, which are a coalescing of more than two wavefunctions [2]. However, for this work we restrict ourselves to "regular" EPs.

[2]Note that $\langle u_i^*| \neq |u_i\rangle^\dagger$

choose (in analogy to the real numbers[3]) the principal square root of z to be $\sqrt{z} = \sqrt{r}e^{i\phi/2}$ (green arrow), then the second branch is $\sqrt{z}' = \sqrt{r}e^{i\frac{\phi}{2}+\pi}$ (blue arrow). There is a branch cut along the negative real axis because $\sqrt{z}$ is not unique when $\phi = \pi$ is approached counterclockwise (upper two panels) or clockwise (lower two panels). To avoid a discontinuous jump, analytic continuation across the branch cut requires an additional phase factor of $e^{i\pi}$, i.e. the two branches $\sqrt{z}$ and $\sqrt{z}'$ are interchanged.
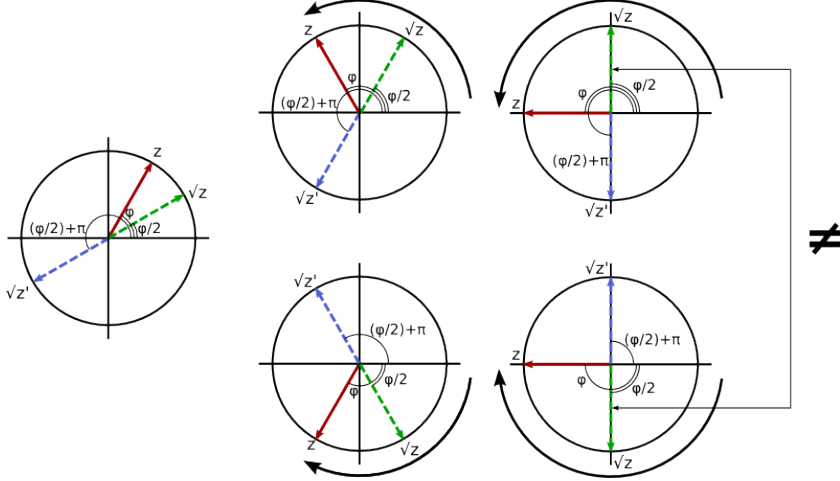

Figure 2.1: Illustration of z (red arrow), the principal value of the square root $\sqrt{z}$ and the secondary branch $\sqrt{z}'$ approaching $\phi = \pi$. The principal value of the square root (green) at $\phi = \pi$ depends upon the the direction of approach. Counterclockwise approaching $\phi = \pi$ results in $\sqrt{z} = exp(i\frac{\pi}{2}) = i$ (top row), whereas approaching $\phi = \pi$ clockwise results in $\sqrt{z} = exp(-i\frac{\pi}{2}) = -i$. This discontinuity is called branch cut.

After making ourselves familiar with the complex square root, we examine the real and imaginary part of λ (as in Eq. (2.4)) as a function of g and ω for fixed γ, as plotted in Fig. 2.2. This figure can also be interpreted as the Riemann surface[4] of the complex square root (with g, ω as $\mathrm{Re}(z), \mathrm{Im}(z)$). The branch cut is situated along the real crossing[5] of λ which is on the negative g-axis. Hence, the branch cut lies where the 'upper' and 'lower' sheet intersect. The color coding in Fig. 2.2 illustrates how the sheets are connected at the real crossing. The EP lies exactly at the beginning of the branch cut.

At the EP the two eigenvalues "coalesce", hence in order to find its position we set the argument of the square root to zero $(\omega + i\frac{\gamma}{2})^2 + g^2 \stackrel{!}{=} 0$. Because the real and imaginary part have to vanish independently, there are actuallly two equations. Requiring the

---

[3]The square root is also multivalued. Usually the principal branch is chosen to be $\sqrt{x} = |\sqrt{x}|$, while the second branch is $\sqrt{x}' = -|\sqrt{x}|$.

[4]Riemann surfaces can be thought of as deformed complex planes, they can be "cut" and "glued" to represent the topological characteristics of a complex function.

[5]A real crossing is a point or line where the real part of the eigenvalues are equal, i.e. cross. Analogously, at an imaginary crossing the imaginary values cross.
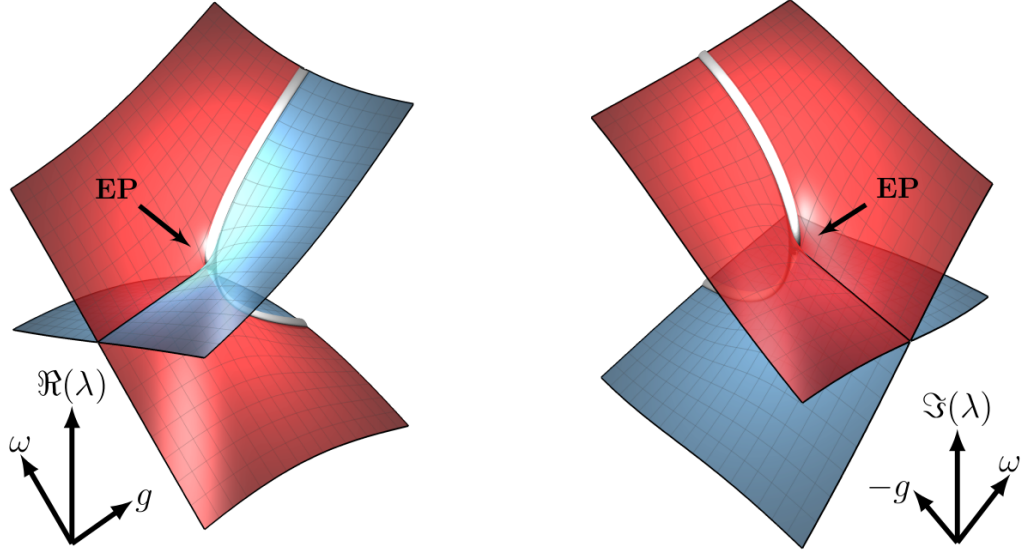
Figure 2.2: Real (left) and imaginary (right) part of the eigenvalue surfaces of $\tilde{H}$ as a function of the parameters g and ω. We can also interpret these surfaces as the real and imaginary part of the Riemann surface of Eq. (2.4) for fixed γ. The color coding highlights the relative gain (red) and loss (blue) of the state (i.e. the imaginary part). This figure is adapted from [7].

imaginary part to vanish leads to $\gamma\omega = 0$ and therefore $\omega_{\mathrm{EP}} = 0$ (ignoring the trivial case of $\gamma = 0$). The real part yields $\omega^2 - \frac{\gamma^2}{4} + g^2 = 0$, resulting in $g_{\mathrm{EP}\pm} = \pm\frac{\gamma}{2}$. Hence, we found two EPs, let's call them EP_+ and EP_-:

$$\mathrm{EP}_+ = (g_{\mathrm{EP}+}, \omega_{\mathrm{EP}+}) = \left(\frac{\gamma}{2}, 0\right) \qquad \mathrm{EP}_- = (g_{\mathrm{EP}-}, \omega_{\mathrm{EP}-}) = \left(-\frac{\gamma}{2}, 0\right) \qquad (2.5)$$

In the beginning of EP-physics people realized that avoided crossings of resonances are always connected with a crossing of the widths of these resonances, as well as a crossing of the levels is connected to a repulsion of the widths [13]. The EP separates the two crossings and is part of both. It is worth to mention that the real part of λ has a crossing $\lambda_+ = \lambda_-$ at $g \in [g_{\mathrm{EP}-}, g_{\mathrm{EP}+}]$, while the imaginary part has a crossing for $g \geq g_{\mathrm{EP}+}$ and $g \leq g_{\mathrm{EP}-}$.

So far, an EP is not much more than a point-degeneracy in a two dimensional parameter space. To emphasize the difference between a degeneracy and an EP we examine the eigenvectors of $\tilde{H}$. At the EP_+ the eigenvectors take the form

$$\langle\lambda_1^*| = \langle\lambda_2^*| = \begin{pmatrix} i & 1 \end{pmatrix} \qquad |\lambda_1\rangle = |\lambda_2\rangle = \begin{pmatrix} i \\ 1 \end{pmatrix} . \qquad (2.6)$$

There is only one eigenvector, and its norm $\langle\lambda^*|\lambda\rangle = 0$ vanishes, the same is valid at the EP_-. Without a full basis available the Hamiltonian is not diagonalizable anymore

and the Hilbert space collapses. At the EP the wavefunctions not only have the same energy, but they are equivalent.

This characteristic of an EP can be used to find them. The Petermann factor [15, 16] is an observable to measure the non-orthogonality of two modes. It becomes large in the vicinity of an EP and diverges at the EP. It is defined as

$$K_{nm} = \frac{\langle u_n^* | u_m^* \rangle \langle v_m | v_n \rangle}{\langle u_n^* | u_n \rangle \langle v_n^* | v_n \rangle} \ . \tag{2.7}$$

With $\langle u_n^* |$ and $|v_m \rangle$ being the n-th left and m-th right eigenvector, respectively, normalized as $\langle u_n^* | v_m \rangle = \delta_{nm}$. For our purposes the mean diagonal Petermann factor

$$\overline{K} = \frac{1}{N} \sum_{n=1}^{N} K_{nn} \ , \tag{2.8}$$

where N is the dimension of the vector space, is well suited. It is equal to one if the eigenvectors are orthogonal and larger in any other case. At the EP the eigenvalues coalesce and the Petermann factor diverges[6] [17, 16]. The Petermann factor for the model Hamiltonian in Eq. (2.3) is shown in Fig. 2.3.
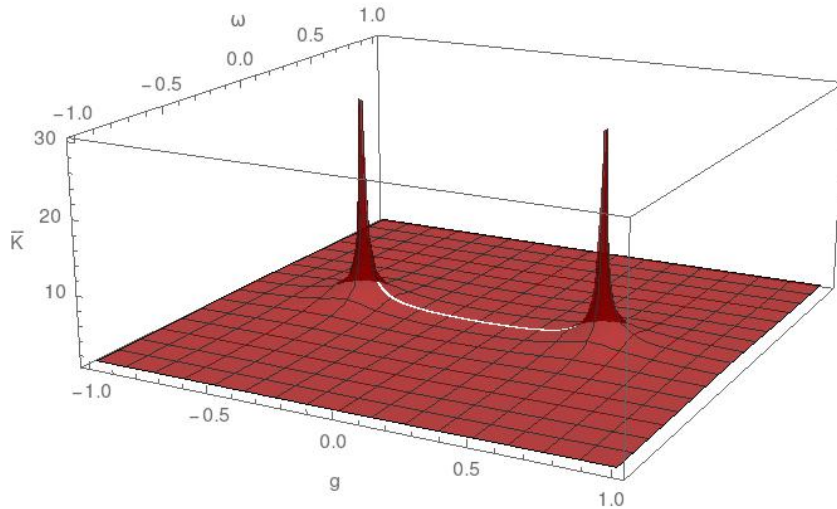

Figure 2.3: Petermann factor for the Hamiltonian in Eq. (2.3) with $\gamma = 1$. The EPs are at $(g, \omega) = (\pm 1/2, 0)$. At the EPs the Petermann factor diverges.

The square root behavior of the eigenvalues $\lambda_\pm$, as in Eq. (2.4), not only makes the energy spectrum inherit the properties of the complex square root, it also makes λ very

---

[6]Because at the EP the hermitian inner product $\langle v_m | v_n \rangle = (|v_m \rangle)^\dagger |v_n \rangle$ does not vanish but the denominator $\langle v_n^* | v_n \rangle$, which is the product of a left and a right eigenvector, is zero.

sensitive to parameter changes around the EPs. In fact, the derivative of λ with respect to the external parameters diverges at the EP.

$$\lim_{g \to g_{\mathrm{EP}}} \frac{\partial \lambda}{\partial g} = \infty \tag{2.9}$$

The physics of exceptional points have attracted a lot of interest. Many demonstrations of EPs have been done using microwave cavities, coupled resonators and optics. Because the ramifications of the EP are vastly different in various systems we refer the reader to further literature [2, 12]. We only want to mention the subtle connection to parity-time ($\mathcal{PT}$) symmetry. Because the eigenvalues of the $\mathcal{PT}$-operator are real, a non-hermitian, $\mathcal{PT}$-symmetric Hamiltonian has entirely real eigenvalues. However, for critical values of the external parameters which characterize the Hamiltonian the $\mathcal{PT}$-symmetry can be spontaneously broken and the eigenvalues become non-real. Indeed, such a critical point is exactly where an EP occurs [2, 12].

The parametric and dynamical encircling of an EP has also received a lot of attention due to the non-trivial topology of the energy level structure around EPs caused by the branch cut. Considering the relevance of this topic for the present thesis, we will discuss it in greater detail in the following section.

2.3 Dynamically encircling an exceptional point

The adiabatic theorem states that a physical system remains in its instantaneous eigenstate if some external parameters are tuned slowly enough and there is always a gap between the state and the rest of the eigenstates [4]. In the case of parameter variations in the vicinity and especially around an exceptional point this implies that the system remains on the "upper" or "lower" sheet, respectively, except at the branch cut where the real parts of the eigenvalues cross. The phase factor $e^{i\pi}$ due to analytic continuation across the branch cut, discussed in the last section, determines that the system changes from the upper sheet of the Riemann surface to the lower one. In the left panel of Fig. 2.4a this means that the state stays on the red sheet.

Hence, naïvely we expect to observe a "state flip" when encircling the exceptional point once [18, 14]. When adiabatically transported around an EP, the state does not return to itself, but ends on the other sheet, as depicted in Fig. 2.4a on the first panel, where the starting and end point are on the lower and upper sheet, respectively. This results in a 4π-periodicity upon variation of these external parameters around the EP, because after a second encircling the state returns to itself.

In reality, this expectation does not hold up to closer examination. The same non-hermicity that is responsible for the emerging of an exceptional point is also responsible for the breakdown of the adiabatic theorem. This is shown in the second panel of Fig. 2.4a, where the starting point is located in a loss area on the upper sheet. In this case, the upper state experiences damping, while the lower one is amplified, which leads to a state change. In other words, the loss-gain structure of the Riemann surface (color coded in Figs. 2.2 and 2.4) either exponentially damps or amplifies a state during time evolution, according to the sign of the imaginary part of the eigenvalue [19]. In this case the non-adiabatic effects cause the state to return back to itself rather than being "flipped" into the lower state.
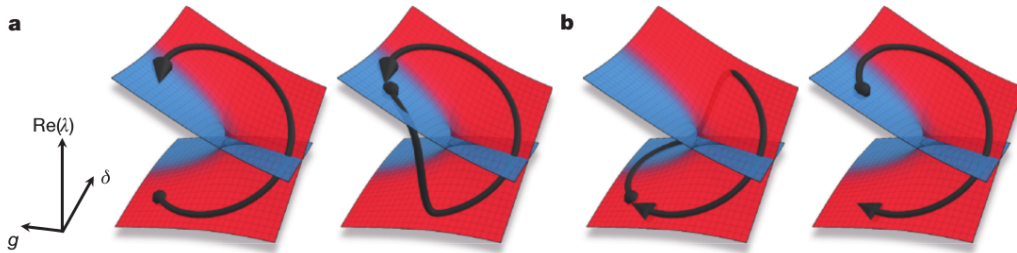

Figure 2.4: Real part of the eigenenergy surface of $\tilde{H}$ with schematic indications of the instantaneous state of the system when encircling the EP. Panels (a) for counter clockwise and panel (b) for clockwise encircling. This figure is taken from [3].

This behavior is turned around when encircling the exceptional point in the other direction (Fig. 2.4b). Hence, the exceptional point shows what we call "chirality". Just like in the example in the previous section, exceptional points often occur in pairs

with different chirality. Encircling both in the same direction (i.e. clockwise) results in opposite states.

To illustrate how adiabaticity breaks down, we assume that g and ω from Eq. (2.3) evolve in time and summarize them as $\vec{q} = (g, \omega) = (g(t), \omega(t)) = \vec{q}(t)$. The following remarks are general, but the notation follows [20].

While $\vec{q}$ evolves in time, let $|n(\vec{q}(t))\rangle$ and $E_n(\vec{q}(t))$ be the instantaneous eigenvectors and eigenvalues, respectively, with n running from one to the dimension of the system. Without loss of generality we can state that at any time t the state $|\Psi(t)\rangle$ can be written as

$$|\Psi(t)\rangle = \sum_n c_n(t) e^{-i\phi_n(t)} |n(\vec{q}(t))\rangle \ , \tag{2.10}$$

where $\phi_n(t) = \int_0^t E_n(\vec{q}(t'))dt'$ is the accumulated phase due to time evolution.

Inserting into the time-dependent Schrödinger equation, $i\partial_t |\Psi(x,t)\rangle = \hat{H} |\Psi(x,t)\rangle$, yields

$$i \sum_n \dot{c}_n e^{-i\phi_n} |n(\vec{q})\rangle = - \sum_n c_n e^{-i\phi_n} \dot{\vec{q}} \nabla_{\vec{q}} |n(\vec{q})\rangle \ . \tag{2.11}$$

For readability we have suppressed the time dependencies. Suppose we prepare the system in a state $|a\rangle$. If the adiabatic theorem holds, then, for sufficiently slow variations the coefficient c_a should dominate over all other amplitudes for all later times. We check if this statement is self-consistent by multiplying Eq. (2.11) with $|b\rangle \neq |a\rangle$ from the left.

$$i\dot{c}_b e^{-i\phi_b} \approx i c_a e^{-i\phi_a} \dot{\vec{q}} \langle b|\nabla_{\vec{q}}|a\rangle \tag{2.12}$$

For this step we have assumed that the eigenstates remain approximately orthogonal. Hence,

$$\dot{c}_b \approx -c_a e^{-i\int_0^t \{E_a(\vec{q}) - E_b(\vec{q})\}dt'} \dot{\vec{q}} \langle b|\nabla_{\vec{q}}|a\rangle \ . \tag{2.13}$$

As long as E_a and E_b are real, the exponential is solely a phase factor and $\dot{c}_b$ can be suppressed by choosing $\dot{\vec{q}}$ arbitrarily small. If, however, E_a and E_b are not purely real there can be exponential growth that cannot be compensated by choosing $\dot{\vec{q}}$ arbitrarily small. Hence, the assumption that the coefficient c_a dominates for all times is not self-consistent anymore.

This phenomenon of adiabatic breakdown due to loss, depicted in Fig. 2.4, can be used to build an asymmetric switch for e.g. electromagnetic waves. It was realized by Doppler et al. [3] for a microwave guide. The adiabatic evolution of external parameters in time is realized by the adiabatic evolution of the boundary conditions of a waveguide in space. The boundary conditions describe a loop around an EP in some parameter space. Hence, traversing the microwave guide in one direction or the other corresponds to moving counterclockwise (Fig. 2.4a) or clockwise (Fig. 2.4b), respectively, along this parameter loop. Subsequently, if a superposition of two modes $|n\rangle$ and $|m\rangle$ enters the waveguide from one side, transmission is high for only one mode, e.g. $|n\rangle$. If the same superposition is inserted from the other side, the mode $|n\rangle$ now becomes suppressed instead of enhanced, and transmission is high for mode $|m\rangle$. This is called an "asymetric switch" (Fig. 2.5).

Figure 2.5: Two modes of a microwave passing a waveguide with modulated boundary conditions. Inserting from the left (right) side corresponds to encircling an EP (counter) clockwise. The waveguide acts as an asymmetric switch because the insertion direction affects which mode passes through. This figure is taken from [3].

The first one to discuss the non-adiabatic processes when encircling an EP was Uzdin et al. 2011 [19], with Gilary et al. 2013 [21] adapting the idea to a physical system. Berry et al. [22] connected the system to the Stokes phenomenon of asymptotics and Milburn et al. 2015 [23] discussed the onset of the non-adiabatic transition, using the theory of stability loss delay. The first experimental confirmation of the effect happened in 2016 by Doppler et al. [3] as already discussed above. Xu et al. demonstrated in 2016 the transfer of energy between two vibrational modes of a cryogenic optomechanical device in laser fields [24].

Most of the studies mentioned so far only consider a very general closed loop around an EP and discuss the chiral behavior when encircling an EP. In his diploma thesis, A. Schumer [7] analytically examines a model system and shows that there exist "phase boundaries" for radii and starting points of EP-centered, circular loops for which encircling the EP yields chirality (Fig. 2.6). An even more striking result is that also loops that do not encircle the EP show chirality [7, 25] (Fig. 2.7). This suggests that the asymmetric switching observed when dynamically encircling an EP is not – as it is often referred to in the literature [18, 14, 24] – a topological effect, but rather a result of a complicated interplay of gain and loss in non-hermitian systems.
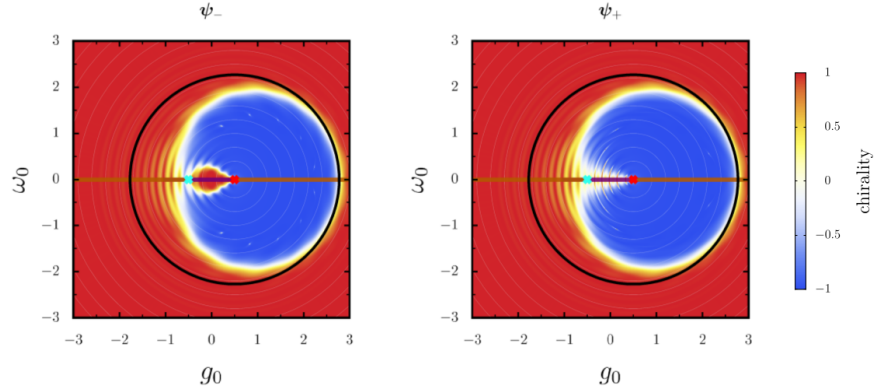
Figure 2.6: Chirality in a system described by the Hamiltonian in Eq. (2.3) with $\gamma = 1$. The color coding describes the chirality (-1) or non-chirality $(+1)$ for circular loops with starting point at (g_0, ω_0), that are centered around the EP_+ (red cross). The left (right) panel shows the initial states ψ_- (ψ_+). The black circle demarcates the approximate boundary between the chiral and non-chiral region. This figure is taken from [7].

When treating adiabatic transport along closed loops, we should also discuss the geometric phase (often called "Berry phase"). Berry showed [26] that a quantum system, which is transported along such a closed loop, picks up a geometric phase according to

$$\gamma_n[C] = i \oint_C \langle n(\vec{q}) | \nabla_{\vec{q}} | n(\vec{q}) \rangle \, d\vec{q}, \tag{2.14}$$

with $\vec{q}$ being coordinates in the space where the loop takes place. The Berry phase is present when encircling an EP, because upon encircling the EP twice (4π-loop) the eigenvalues return to their initial values (disregarding non-adiabatic effects) but the eigenvectors pick up a minus sign. Hence, while the eigenvalues show a 4π periodicity, the eigenvectors are 8π-periodic.

$$|\psi_+\rangle \xrightarrow{2\pi} |\psi_-\rangle \xrightarrow{2\pi} -|\psi_+\rangle \xrightarrow{2\pi} -|\psi_-\rangle \xrightarrow{2\pi} |\psi_+\rangle \tag{2.15}$$

This is a manifestation of a Berry phase of exactly $\gamma = \pi$ for the double circle [27]. When we numerically simulate the encircling of an EP, the geometric phase is implicitly taken care of.
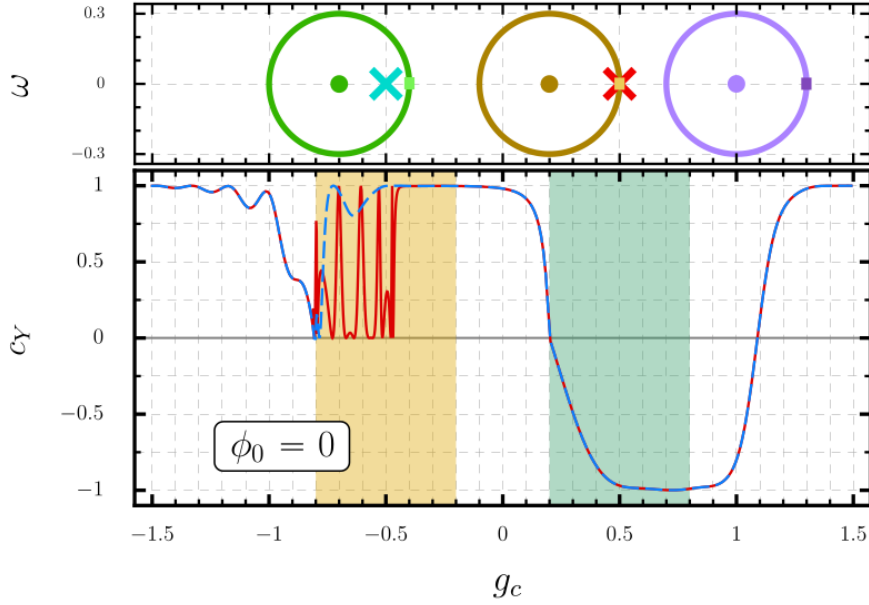
Figure 2.7: This figure illustrates the chirality for a circular loop with fixed radius at variable positions. The upper panel shows three illustrative loops with centers at $(g, \omega) = (g_c, 0)$ and the start position marked by a small rectangle. The EPs are displayed as colored crosses. The bottom panel shows the chirality ($c_Y = -1$ for a chiral loop, $c_Y = +1$ for a non-chiral loop) for circular loops with $r = 0.3$ and centered at $(g, \omega) = (g_c, 0)$ for an initial loss state ψ_- (blue, dashed line) and an initial gain state ψ_+ (red, solid line). The areas where the circle encloses the EP are shaded green or yellow. Note that chirality prevails up until a value of g_c where no EP is encircled (purple circle in the upper panel). This figure is taken from [7].

3 Graphene

In the previous chapter we motivated non-hermitian mechanics and explained what exceptional points are. This chapter is dedicated to the second half of the title "Exceptional points in graphene nanoribbons". We will introduce the reader to graphene and its electronic structure, its connection to non-hermitian physics and the characteristics of graphene nanoribbons.

Pure carbon occurs in nature in two crystalline forms. Its most famous form is of course diamond, used in jewelery for its rareness as well as in cutting and drilling for its hardness and great ability to conduct heat. The other phase occurring in nature is graphite. While diamond is the hardest existing mineral, graphite is very soft. It is used for electrodes in batteries and various other purposes, probably the most familiar one being writing with pencils.

Graphite consists of layers of carbon atoms that have covalent bonds in plane and are only weakly bound by van-der-Waals forces out of plane. In 2004 Geim and Novoselov [5] were able to remove such a single plane of carbon atoms from graphite. This material is today know as graphene. Their discovery not only showed the remarkable properties of graphene, but turned out to be the spark that ignited the whole field of "two dimensional materials". They were awarded with the Nobel prize in 2010.

The electronic configuration of carbon is $[\text{He}]2s^2 2p^2$, but for molecular carbon the $2s$ and $2p$ orbitals containing the four chemically active electrons hybridize in different combinations. Graphene has exceptional mechanical strength due to σ-bonds formed by sp^2 orbitals, but is even more famous for its electronic properties, which we will investigate in the following chapter.

After its discovery a lot of research has been invested in the fabrication and theoretical understanding of graphene and devices made thereof. Nowadays, very clean and large samples [28] as well as atomically precise graphene ribbons can be fabricated [29]. This makes graphene an attractive playground to test ideas and effects not only valid for graphene, but also for the whole class of 2D-materials.

3.1 The electronic structure of graphene

As already mentioned, we find the carbon atoms of graphene in their sp^2 hybridization. Hence, they form a hexagonal honeycomb lattice with a 120° angle between the bonds. The crystal structure is depicted in the left panel of Fig. 3.1. The sp^2 orbitals mix with the neighbouring orbitals and form bonding and antibonding σ bonds[1]. The binding sp^2 orbitals are fully occupied, which leaves a single electron in the p_z at every carbon site, making it half-filled. It is safe to assume that the overlap of the p_z orbitals is small, as they extend mainly into the z-direction. Hence, it is natural to choose a tight binding ansatz using only the p_z orbitals [30, 31]. For didactic reasons the calculations in this section are performed using only nearest neighbor hopping.
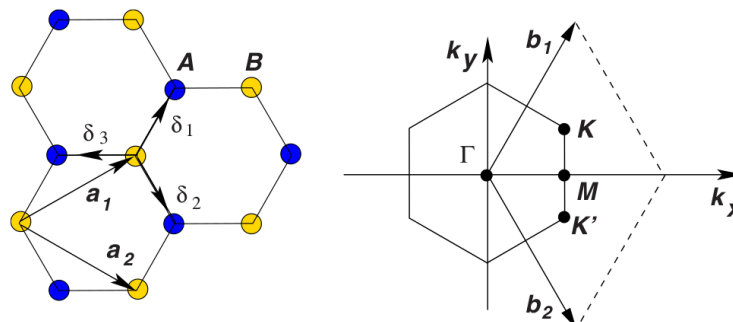
Figure 3.1: *Left panel:* Real space structure of graphene. The two sublattices are denoted A and B, a_1 and a_2 are the lattice vectors and δ_i are the nearest neighbor vectors. *Right panel:* The first Brillouin zone of graphene. The reciprocal lattice vectors are denoted by b_1 and b_2. Note that there are two corners of the Brillouin zone K and K' that are not connected by an a lattice vector. Figure extracted from [31].

Before writing down the tight binding Hamiltonian we need to establish some geometrical prerequisites. Graphene crystallizes in a hexagonal structure, which is basically a trigonal unit cell with a diatomic basis or, expressed differently, two inequivalent trigonal sublattices A and B. It is depicted in Fig. 3.1. We define the unit vectors for the Bravais lattice as

$$\vec{a}_1 = \frac{a}{2}(3, \sqrt{3}), \qquad \vec{a}_2 = \frac{a}{2}(3, -\sqrt{3}), \tag{3.1}$$

where $a \approx 1.42\text{Å}$ is the carbon-carbon bond length. The three nearest neighbor vectors are

$$\vec{\delta}_1 = \frac{a}{2}(1, \sqrt{3}), \qquad \vec{\delta}_2 = \frac{a}{2}(1, -\sqrt{3}), \qquad \vec{\delta}_3 = -a(1, 0). \tag{3.2}$$

---

[1]Chemistry differentiates covalent bonds by their symmetry. For example a σ bond formed by the mixing of two orbitals has rotational symmetry around the atom-atom axis. In contrast a π bond, as formed for example by overlapping p_z orbitals, is characterized by an electron density of zero in a common nodal plane.

Suppose t is the overlap integral[2] ("hopping integral") of two p_z orbitals. By symmetry it has to be the same for all three nearest neighbor pairs. With these definitions we can write down the tight binding Hamiltonian for graphene,

$$H = -t \sum_{\langle ij \rangle, \sigma} a_{i\sigma}^\dagger b_{j\sigma} + h.c. \; , \tag{3.3}$$

with $a_{i\sigma}^\dagger$ ($a_{i\sigma}$) creating (annihilating) an electron with spin σ in the p_z orbital on the A sublattice of the unit cell at $\vec{R}_i$. The same definition is valid for creation (annihilation) on the sublattice B $b_{i\sigma}^\dagger$ ($b_{i\sigma}$). The first term represents the "hopping" of an electron on an atom of sublattice A to one of its neighbors on sublattice B, the second term $h.c.$ denotes the hermitian conjugate of the first term, and therefore the hopping of an electron from a B to a A site.

It is helpful to write the Hamiltonian more explicitly to work with it later,

$$H = -t \sum_{i,\sigma} a_{r_i\sigma}^\dagger b_{r_{i+\delta_1}\sigma} + a_{r_i\sigma}^\dagger b_{r_{i+\delta_2}\sigma} + a_{r_i\sigma}^\dagger b_{r_{i+\delta_3}\sigma} + h.c. \; . \tag{3.4}$$

To make use of the Bloch's we perform a 2D Fourier transform, this represents the problem in reciprocal space ("k-space"). The unit vectors of the first Brillouin zone (see Fig. 3.1 right panel) evaluate by their definition $\vec{a}_i \cdot \vec{b}_j = 2\pi \delta_{ij}$ to

$$\vec{b}_1 = \frac{2\pi}{3a}(1, \sqrt{3}), \qquad \vec{b}_2 = \frac{2\pi}{3a}(1, -\sqrt{3}). \tag{3.5}$$

The 2D Fourier transformation is defined as

$$c_j = \frac{1}{\sqrt{N}} \sum_{\vec{k}} c_k e^{i\vec{k} \cdot \vec{r}_j} \tag{3.6}$$

$$c_{\vec{k}} = \frac{1}{\sqrt{N}} \sum_j c_j e^{i\vec{k} \cdot \vec{r}_j} \; , \tag{3.7}$$

with $c = a, b$. Inserting (3.6) into (3.4) and using the identity

$$\frac{1}{N} \sum_j e^{-i(\vec{k} - \vec{k}')\vec{r}_j} = \delta_{kk'} \tag{3.8}$$

leads to

$$H = -t \sum_k \begin{pmatrix} a_k^\dagger & b_k^\dagger \end{pmatrix} \underbrace{\begin{pmatrix} 0 & H_{12} \\ H_{21} & 0 \end{pmatrix}}_{\mathcal{H}_0} \begin{pmatrix} a_k \\ b_k \end{pmatrix}, \tag{3.9}$$

where $\mathcal{H}_0$ denotes the kernel of the Hamiltonian. Its matrix elements are

$$H_{12} = H_{21}^* = e^{i\vec{k} \cdot \vec{\delta}_1} + e^{i\vec{k} \cdot \vec{\delta}_2} + e^{i\vec{k} \cdot \vec{\delta}_3}. \tag{3.10}$$

---

[2]The numerical value of t is typically $t \approx 2.8\,\text{eV}$ [31], although it is not important for the properties presented here.

We can calculate the eigenenergies by diagonalizing the kernel $\mathcal{H}_0$. The eigenenergies are given by

$$\epsilon_\pm(\vec{k}) = \pm|t|\sqrt{3 + 2cos(\sqrt{3}k_y a) + 4cos(\frac{3}{2}k_x a)cos(\frac{\sqrt{3}}{2}k_y a)} \tag{3.11}$$
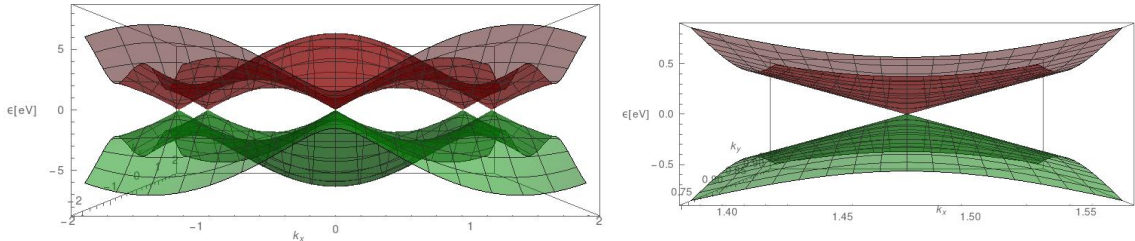
and represented in Fig. 3.2.

Figure 3.2: Bandstructure of graphene. *Left panel:* Bandstructure of graphene in the nearest neighbor tight binding approximation. The cones touch at the corner of the Brillouin zone. There are only two independent corners K, K' of the Brillouin zone that are not connected by an inverse lattice vector, hence the six cones visible reduce to two inequivalent cones. *Right panel:* Zoom of the K point. Around the Fermi energy $\epsilon = 0$ the bandstructure is perfectly conical and, hence, linear.

Exactly at the corners of the Brillouin zone, denoted K and K' in Fig. 3.1, the filled upper and lower bands touch (see Fig. 3.2). The lower band is completely filled and the upper band is completely empty. This makes graphene a semi-metal: It does not have a band gap, but the density of states at the Fermi energy is zero. The K and K' points are located at

$$\vec{K} = \left(\frac{2\pi}{3a}, \frac{2\pi}{3\sqrt{3}a}\right), \qquad \vec{K}' = \left(\frac{2\pi}{3a}, -\frac{2\pi}{3\sqrt{3}a}\right). \tag{3.12}$$

In Fig. 3.2, the right panel shows a zoom of the K point. The dispersion relation does not exhibit the parabolic bandstructure of a free electron but it is linear in a large energy window around the Fermi energy E_F. This resembles much more the linear dispersion relation of a massless (relativistic) Dirac fermion. For that reason the touching point of the upper and lower band is often called the Dirac point. The analogy between the quasi-particles in graphene and relativistic fermions has been used to test ideas from quantum electrodynamics, for instance the first experimental realization of Klein tunneling [32] was done using graphene.

Since there are two inequivalent K-points (see Fig. 3.1) and the energy gap between them is relatively large (compare with Fig. 3.2), the K/K'-degree of freedom serves as an additional quantum number called the 'valley'.

When second or higher order nearest neighbor hopping terms are included the electron-hole symmetry is lifted. Then, the upper and lower band in Fig. 3.2 are not symmetric anymore. For the calculations of the nanoribbons in this thesis we employ a third nearest neighbor hopping model and the recursive Greens function method in an implementation by Libisch et al. [33].

The remarks on the electronic properties of graphene presented in this chapter are limited by the scope of this work, for a more comprehensive treatment of the electronic properties of graphene see the excellent review by Castro Neto et al. [31].

3.2 Towards non-hermitian effects in graphene

This section will present how to evoke and describe non-hermitian effects in graphene. As a first step we include real on-site terms. Imagine that the A and B atoms sit on top of different atoms, then the inequivalent sublattices will experience different (constant) on-site potentials, represented in the tight binding Hamiltonian as diagonal terms $V_{A,B}$. The following equation shows how such an on-site potential can be rewritten into a sublattice independent term $V_0 = (V_A + V_B)/2$ and a sublattice dependent term $V_z = (V_A - V_B)/2$,

$$\mathcal{H} = \mathcal{H}_0 + \begin{pmatrix} V_A & 0 \\ 0 & V_B \end{pmatrix} = \mathcal{H}_0 + \begin{pmatrix} V_0 & 0 \\ 0 & V_0 \end{pmatrix} + \begin{pmatrix} +V_z & 0 \\ 0 & -V_z \end{pmatrix} = \mathcal{H}_0 + V_0\sigma_0 + V_z\sigma_z . \quad (3.13)$$

The subscripts of the transformed on-site potentials refer to the Pauli matrices σ_0 and σ_z. The sublattice-independent on-site term V_0 shifts the overall energy scale locally, but does not have an effect on the dispersion relation itself. On the other hand, the sublattice dependent on-site term V_z has an effect on the bandstructure by opening a gap at the K and K' points (as shown in Fig. 3.3). Because this is equivalent to introducing a mass term in the Dirac equation, the V_z term is sometimes called a "mass term".
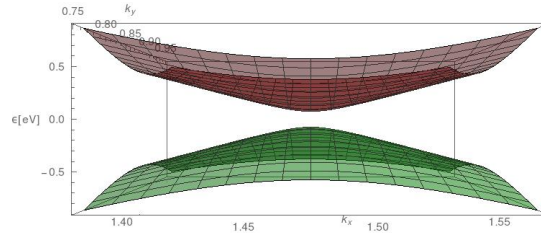

Figure 3.3: Bandstructure of graphene around the K point. The degeneracy at the Dirac point is lifted by a mass term of $V_z = 0.1$eV.
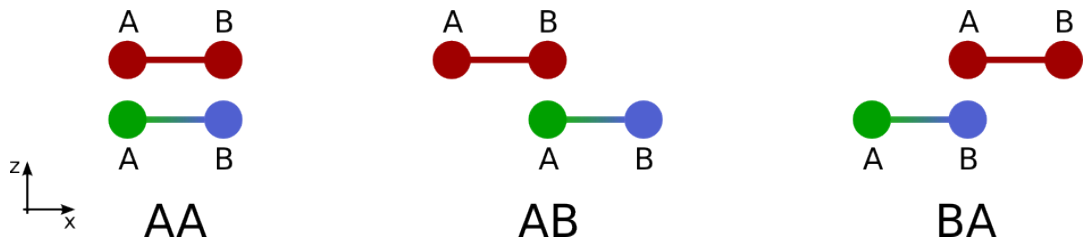

Figure 3.4: Unit cell of graphene (red) stacked on hexagonal boron nitride (green and blue) in various stacking configurations. The carbon atoms of sublattice A and B will not have the same tunneling probability to an underlying substrate for any two of the stacking configurations.

As already mentioned in chapter 2, we can implement an effective model of gain and loss by including imaginary terms $i\Gamma$ in the diagonal of the Hamiltonian[3]. The

---

[3]The magnitude of Γ will be approximately proportional to the overlap of the orbials that come into question.

tunneling rate Γ will, in general, not be the same for both sublattices A and B. Imagine a graphene flake stacked on hexagonal boron nitride on a conducting substrate. The tunneling rate for to the conductor will depend on the stacking configuration (compare with the illustration in Fig. 3.4). Hence, we assume the on site potentials $V_A \neq V_B$ and consequently V_0 and V_z to be complex numbers (i.e. we absorb $i\Gamma$ into the potentials).
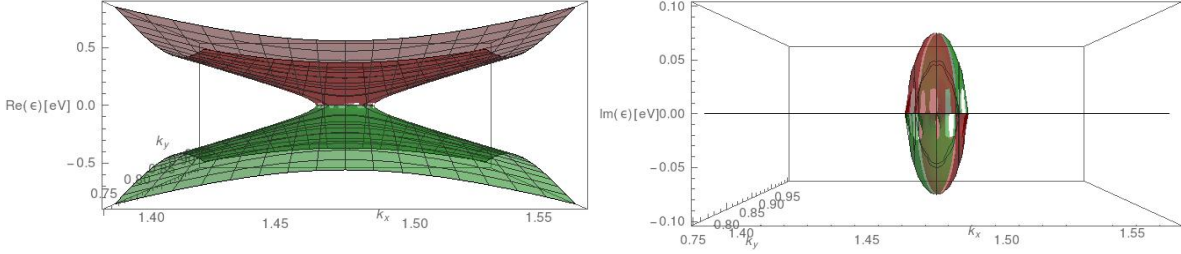

Figure 3.5: Zoom of the K point for graphene with a complex sublattice splitting potential of $V_z = i0.1$eV. In contrast to a real V_z (Fig. 3.3) the cones move towards each other. Inside of the circular intersection line the eigenvalues are purely imaginary. The intersection line is a ring of exceptional points.

The effect of a complex sublattice splitting potential can be seen in Fig. 3.5. While a real V_z introduces a gap, an imaginary V_z moves the dirac cones into each other, making the eigenvalues purely imaginary inside the circular boundary where the cones intersect. The points on the intersection line are exceptional points. Hence, sublattice dependent gain and loss introduces a "ring of exceptional points" in graphene, that has already been observed in similar systems [10]. To convince ourselves that this ring is constituted by EPs we calculate the Petermann factor. Figure 3.6 shows how the average Petermann factor $\overline{K}$ diverges at the circle where the two cones intersect. Hereby, we have shown that graphene has exceptional points. In the next sections we will investigate whether they are accessible in experiment.
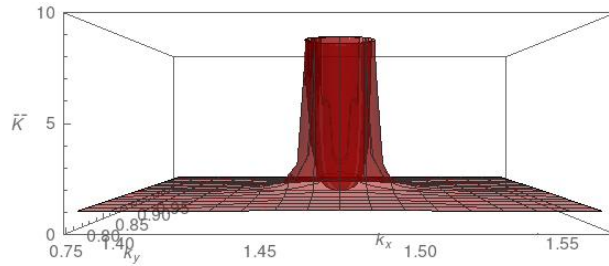

Figure 3.6: Petermann factor for the same parameters and zoom of the bandstructure as in Fig. 3.5. The Petermann factor diverges at the circle where the Dirac cones intersect. This indicates that we observe a ring of exceptional points.

3.3 Graphene nanoribbons

In the discussions above we assumed bulk graphene, extending infinitely in both directions. However, in an experiment (investigating transport) one usually considers nanoribbons that extend much further in one direction than in the other. Theoretically we imagine this by cutting strips out of pristine graphene. There are two major directions as shown in Fig. 3.7. One edge is called zigzag and the other one armchair. Since the Bloch theorem is only valid in one direction, the Brillouin zone is only one dimensional too. The constriction in the other direction shows up as additional levels in the band structure[4]. The two kinds of graphene nanoribbons have very distinct bandstructures, which we will discuss in the following.
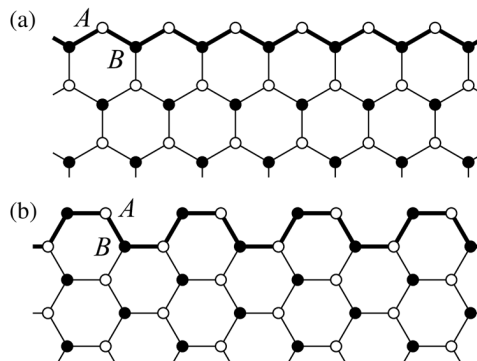
Figure 3.7: Different edge terminations of graphene nanoribbons. *(a)* Zigzag edge. *(b)* Armchair edge. Taken from [34].

A ribbon like the one displayed in Fig. 3.7(b) that extends infinitely in the x direction is called armchair ribbon. Because the Bloch theorem holds only in x direction (the material is not periodic in the y-direction anymore) the two inequivalent cones depicted in Fig. 3.2 are projected onto each other [31]. The resulting dispersion relation (see Fig. 3.8) has a small gap at the K and K' points that is inversely proportional to the width of the nanoribbon [35, 36, 37].

On the other hand, when the ribbon displayed in Fig. 3.7(a) extends in macroscopically (infinitely) in x direction it is called zigzag. Because the constriction, and, hence, quantization, is orthogonal to the armchair case the cones are not projected onto each other (see Fig. 3.1 and Fig. 3.9). It is noteworthy that zigzag ribbons feature a topologically protected edge state [31]. In a nearest neighbor description the edge state is dispersionless, but when higher order neighbor hoppings are included (i.e. particle-hole symmetry is broken) the edge state becomes weakly dispersive.

---

[4]This is because the dimension of the kernel (3.9) will now be the number N of atoms in the direction of the constriction. This gives N eigenvalues for every k that point into the other direction.
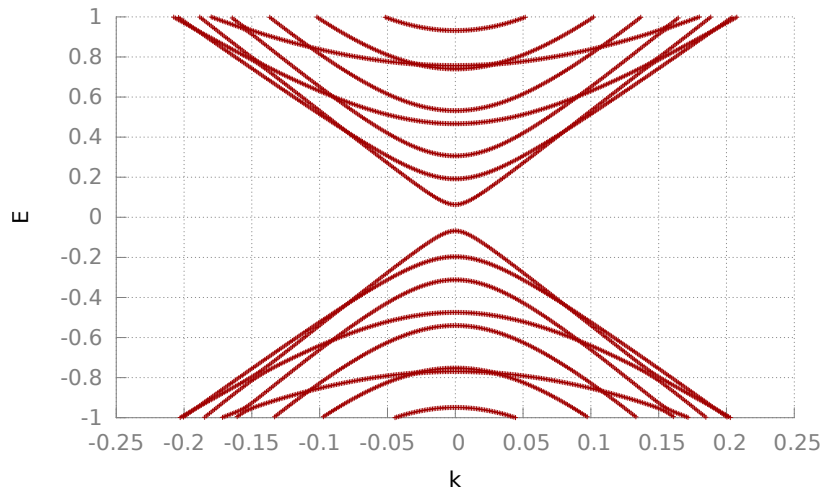
Figure 3.8: Bandstructure for an armchair nanoribbon with a width of $w = 61\text{Å}$ in a third nearest neighbor TB-description. The two Dirac cones are superimposed and at $k = 0$ a gap forms.
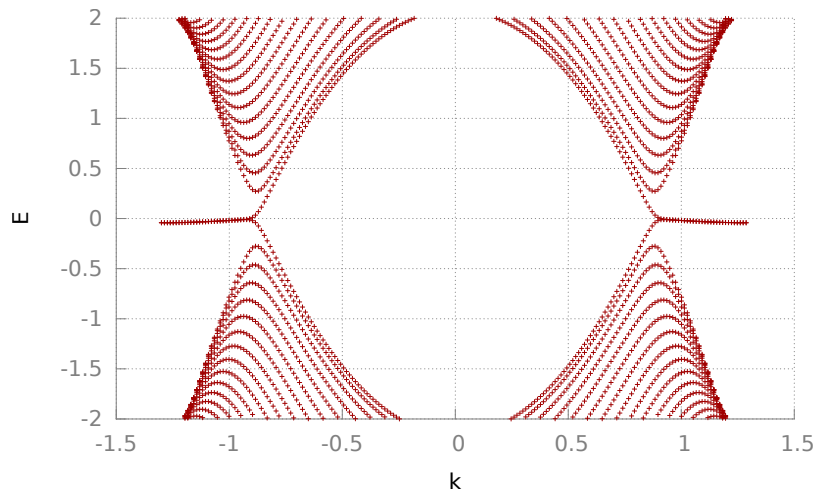

Figure 3.9: Bandstructure for a zigzag nanoribbon with a width of $w = 85\text{Å}$ in a third nearest neighbor TB-model. The Brillouin zone is rotated with respect to the armchair case, therefore the K and K' cones are not superimposed. The edge state (energy level at $E \approx 0$ connecting the two cones) is topologically protected and prevents a gapless spectrum.

4 Riemann surfaces

The first part of this work was to investigate the Riemann surface structure of graphene or rather graphene nanoribbons. A Riemann surface visualizes the structure and connections of the complex eigenvalues as a function external parameters. They are useful tool when proving the existence of exceptional points and determining their location. This chapter first discusses which parameters can be varied, then presents the steps necessary to "draw" a Riemann surface that is analytically not accessible. The section thereafter presents our results for different edge terminations and different parameter combinations.

All the energies and potentials in this chapter are given in electron volt. We omit them for clarity.

4.1 Parameter space

Without an experiment to reproduce, it is not straightforward to decide which parameters to vary and in what range to vary them. For graphene, comparing Eqs. (2.3) and (2.4)

$$\tilde{H} = \begin{pmatrix} -\omega - i\frac{\gamma}{2} & g \\ g & \omega + i\frac{\gamma}{2} \end{pmatrix} \quad \text{and} \quad \lambda_\pm = \pm\lambda = \pm\sqrt{(\omega + i\frac{\gamma}{2})^2 + g^2},$$

with Eq. (3.13)

$$\mathcal{H} = \mathcal{H}_0 + V_0\sigma_0 + V_z\sigma_z = \begin{pmatrix} V_0 + V_z & tH_{12} \\ tH_{12}^* & V_0 - V_z \end{pmatrix},$$

using H_{12} as defined in Eq. (3.10) and $V_z = V_z^0 + i\Gamma$, yields

$$\epsilon_{\text{Graphene}} \propto \sqrt{t^2 \cdot H_{12}^2 + (V_z^0 - i\Gamma)^2} \, . \tag{4.1}$$

This suggests to vary two out of three of the real sublattice splitting potential V_z^0, the sublattice dependent gain/loss rate Γ and the hopping parameter t. There are of course other parameters that could be varied, which are not included explicitly in this formula such as energy, the width of a ribbon or the magnetic field. Because calculating the bandstructure of graphene nanoribbons analytically is not possible, we employ numerical simulations.

We want to provide a physical interpretation of the parameters that can be varied and explain the connection to experiment. For example, here the sublattice splitting potential consists of a real and imaginary part $V_z = V_z^0 + i\Gamma$. The real part V_z^0 represents

the on-site energy, i.e. the chemical environment. The imaginary part $i\Gamma$ represents the tunneling probability or effective gain or loss, respectively. With this interpretation we can concieve a hypothetical device depicted schematically in Fig. 4.1. A graphene flake is separated from another graphene flake (or a graphite crystal) by a single layer of an insulator (e.g. hBN). Between the two layers a voltage $V_{\text{tunneling}}$ introduces a tunneling current. If the substrate has the same crystal structure but with two inequivalent elements or AB/BA stacking (compare with 3.4), the on-site energy and tunneling current will not be the same for both sublattices (compare with Fig. 3.4). With a spectroscopic method or two contacts at the graphene flake experiments can be conducted as a function of $V_{\text{tunneling}} \propto \Gamma$.
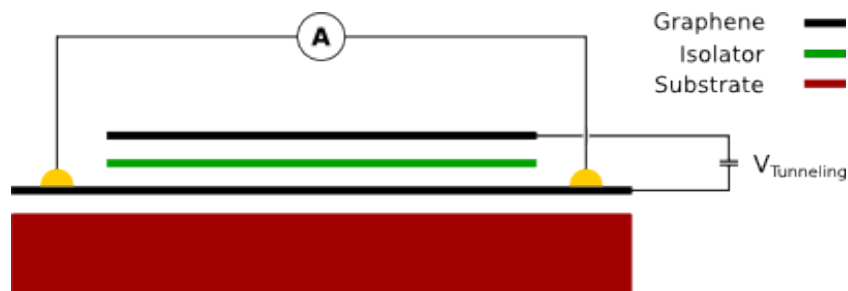

Figure 4.1: Sketch of the proposed device. Two graphene flakes (black) are separated by a single or a few layers of an insulator. The graphene flakes will be connected via tunneling which can be controlled by varying the number of insulating atom-layers or tuning the tunneling voltage $V_{tunneling}$. Measuring the conductivity for one of the flakes yields information about the transmission probability.

It is harder to imagine experiments where the chemical on-site potential is varied dynamically. However, in moiré superstructures (see Fig. 4.2, left panel), forming, e.g., when graphene is placed on hexagonal boron nitride, the sublattice splitting potential varies as a function of the position inside this superstructure [38, 39].

A different approach to creating an alternating potential is placing the graphene on a surface that has reconstructed in a way similar to a washboard. Such a surface could be the "missing row" reconstructed gold or platinum (110) surface (compare with Fig. 4.2, right panel). The graphene ribbon will then experiences a different local potential in the form of a grating. We will call a potential generated by such a structure 'grating potential' $V_{grating} \equiv V_g$.

Modulating the hopping parameter t in an experiment is generally associated with changing the lattice constant by strain. Of course one has to be careful, because this also generates a phase[1], analogous to a magnetic field [41, 42]. Limited by the scope of this thesis, we avoid this complication and only show that varying t yields an exceptional point, while we mainly focus on other parameters.

There is one last parameter that is only included implicitly, the width w of the nanorib-

---

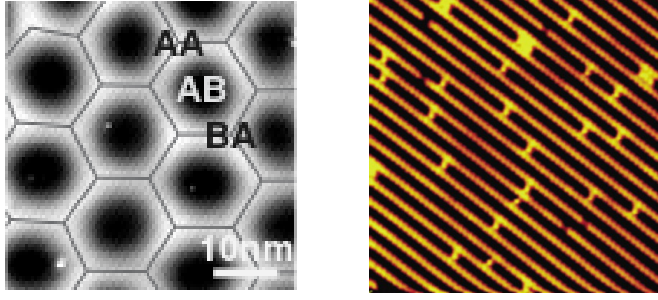[1]Because in Eq. (3.9) the nearest neighbor vectors in H_{12} change.

Figure 4.2: *Left panel:* Scanning tunneling microscope topography (constant current mode) of graphene on hBN. The resulting superstructure with a lattice constant of $\gtrsim$ 100nm is clearly visible. Fig. taken from [39]. *Right panel:* STM image showing the Pt(110)(12) surface in the missing-row reconstruction with single adatoms and small islands. The imaged area is $140 \times 140 \text{Å}^2$. Figure taken from [40].

bons. In general, the width determines the magnitude of the level spacings of the ribbon[2], as well as the size of the gap around the Fermi energy. The level spacings and the gaps decrease for wider ribbons (compare with Sec. 3.3 and Refs. [35, 36, 37]). Figure 4.3 shows the width of a ribbon vs. the position of the EP, for the energy fixed at $E = 0.1$. For increasing ribbon-width the potential value at the EP decreases. At approximately $w \approx 220\text{Å}$ the EP vanishes, because the fixed energy is no longer inside the gap.
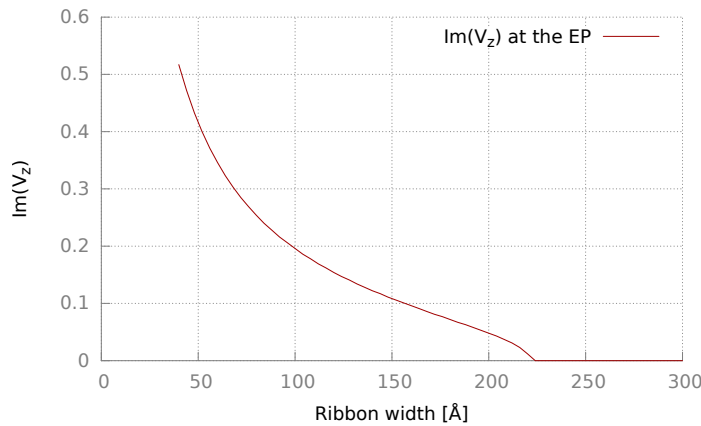

Figure 4.3: Position of the EP of a zigzag ribbon vs. the width of the ribbon. We plot $\text{Im}(V_z)$ because the EP is always on the imaginary axis ($\text{Re}(V_z) = 0$). The energy is fixed at $E = 0.1$ inside the gap. Hence, for widths larger than $w \approx 220\text{Å}$ there is no EP, because the energy is not in the gap anymore. If the energy would be fixed at $E = 0.0$ the curve would extend much further.

---

[2]We can compare the narrow constriction of the nanoribbon to to the one dimensional potential well. There the level spacings are also proportional to $1/L$.

4.2 Inverse bandstructures

The most straightforward way to study exceptional points as a theoretician is by examining the Riemann surface of two energy levels. It yields whether there is an exceptional point, where it is and potentially other non-trivial features. This section explains how to "draw" a Riemann surface and establishes the principles that are common to all the Riemann surfaces presented in the following section.

Naïvely, the first step to draw a Riemann surface is to track the evolution of the energy of a certain state according to some external parameter. However, this work was also aimed to explore dynamics in the presence of exceptional points. Instead of varying some external parameters adiabatically in time, we use a scheme inspired by Doppler et. al. [3] (see chapter 2). The boundary conditions of a graphene nanoribbon are varied along the length of the nanoribbon and an electron propagating through the ribbon experiences changing boundary conditions. Therefore, the place of the time evolution operator $U(t) = exp(iEt/\hbar)$ is taken by Bloch's phase, which allows us to define an operator for the "time-evolution" where the position x takes the role of time[3] $U(x) = exp(ikx)$. If x takes the role of time, the crystal momentum k takes the role of the energy E. Hence, we are not interested in the Riemann surface for the energy, but for the quasi-momentum k. This is possible by solving the inverse problem of finding the crystal momentum k for a fixed energy. In solid state physics usually bandstructures $E(k)$ are studied, but to draw Riemann surfaces for the problem at hand we need to consider the inverse bandstructure $k(E)$. The following paragraphs will highlight the differences between a bandstructure and an inverse bandstructure.
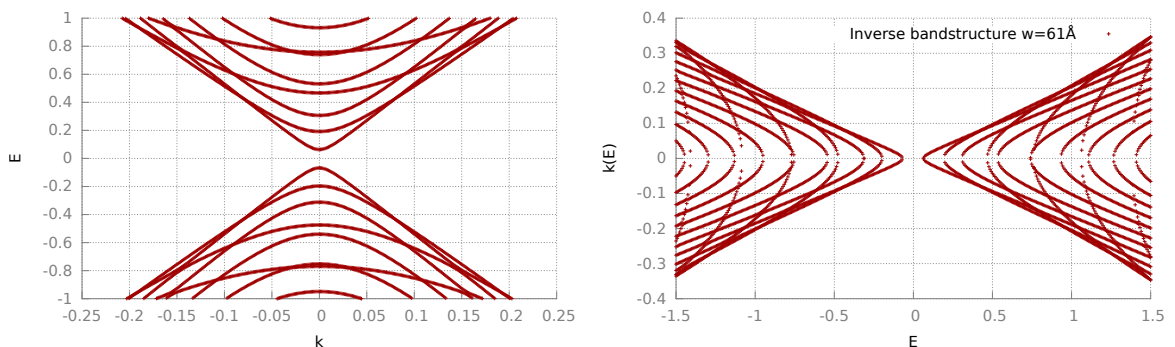

Figure 4.4: *Left:* Bandstructure $E(k)$ for a 102 atoms wide graphene nanoribbon. *Right:* Inverse bandstructure $k(E)$ for the same ribbon, showing only the real eigenvalues.

The inverse bandstructure is in a few aspects different to a 'regular' bandstructure. When solving the $N \times N$-Hamiltonian for $E(k)$, it has N real eigenenergies for every k. According to the right panel of Fig. 4.4 the inverse problem apparently does not

---

[3]In the following we will calculate stationary scattering states. Because the energy is kept real, "regular" time evolution will only contribute a phase factor and we do not need to worry about exponential growth or decay due to complex energies.

have the same number of results for every energy. Inside the gap there are no (real) eigenvalues at all. This is because Fig. 4.4 shows only the real eigenvalues of the inverse problem, which is actually not limited to the real eigenvalues. This can be seen by inserting Bloch's theorem

$$\psi(x) = e^{ikx} u_k(x) \tag{4.2}$$

into the time-independent Schrödinger equation

$$\left(\frac{\hbar}{2m} \frac{\partial^2}{\partial x^2} + V(x) \right) \psi(x) = E\psi(x) \ . \tag{4.3}$$

This leads to

$$\frac{\hbar}{2m} (u''(x) + 2iku'(x) - k^2 u(x)) + V(x)u(x) = Eu(x) \ , \tag{4.4}$$

the equation which needs to be solved for the inverse problem. The solutions for k don't need to be real because the differential operator is not self-adjoint anymore. When the complex eigenvalues of the inverse problem are included, it has $2N$ solutions, because k appears squared in eq. (4.4). In Fig. 4.5 all the solutions of the inverse problem are included. Physically, the complex eigenvalues represent localized states, because the Bloch factor (Eq. (4.2)) with a complex k does not propagate the electron along the ribbon, but represents an exponential decay. At this point it becomes clear that the bandstructure and the inverse bandstructure are not the same problem solved differently, but especially in the case of a non-hermitian potential $V(x)$, they are different problems[4].
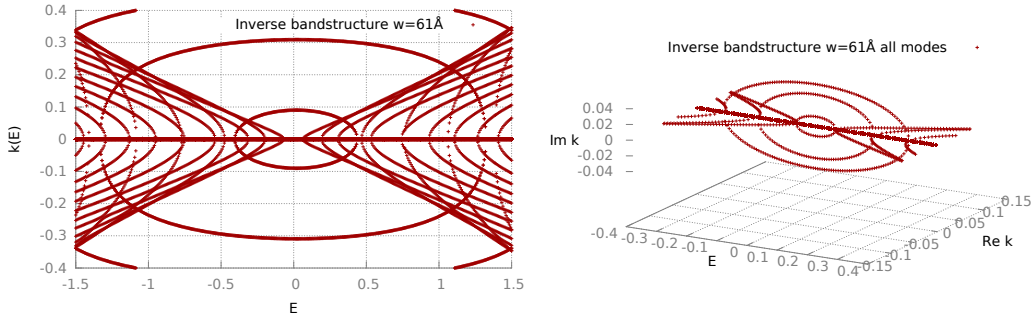

Figure 4.5: Inverse bandstructure $k(E)$ including all eigenvalues for a 102 atoms wide graphene nanoribbon. *Left panel:* Real part $\mathrm{Re}(k(E))$ of the eigenvalues. *Right panel:* Zoom to the Dirac point, same as the left panel, but with the imaginary part $\mathrm{Im}(k(E))$ plotted as z-axis.

In order to draw a Riemann surface, we record the evolution of the complex eigenvalue for a fixed energy $k(E)$ when varying some external parameters. The external parameters can be chosen freely, compare with the discussion in the previous section. An exemplary

---

[4]In practice this can be seen for instance when the 'regular' and inverse problem both show EPs, but at completely different parameter combinations. One could say that we consider different three-dimensional cuts through the four-dimensional space spanned by $\mathrm{Re}(k)$, $\mathrm{Im}(k)$, $\mathrm{Re}(E)$ and $\mathrm{Im}(E)$.

Riemann surface for an armchair ribbon is depicted in Fig. 4.6. It shows the sign of the imaginary part of the respective eigenvalue as color coding, with red (green) being a gain (loss) state. The EP is situated on the imaginary axis and is connected to a second EP, that is mirrored across the real axis, by a real crossing (as opposed to an imaginary crossing, like the one starting at the EP and going to negative imaginary infinity).
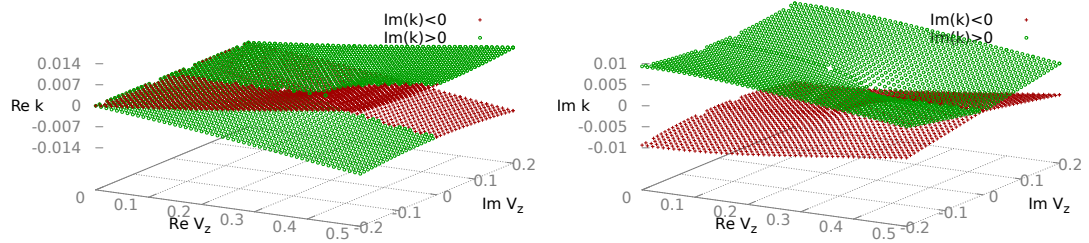

Figure 4.6: Riemann surface for the bandstructure in Fig. 4.5. The color coding represents the sign of the imaginary part, red (green) representing gain (loss). *Left panel:* Real part of the k-eigenvalue. *Right panel:* Imaginary part of the k-eigenvalue.

4.3 Results

After establishing how to determine them, this section presents the Riemann surfaces for various parameter combinations. We will start with armchair ribbons with complex grating potential and discuss generic and non-generic EPs. Then we will discuss a complex sublattice splitting potential for zigzag ribbons, representative for both armchair and zigzag ribbons. In this theoretical study we present typical cases, which of course would need to be adapted for a certain device.

4.3.1 Armchair with grating potential

We start with an armchair ribbon that is placed on a surface in the missing-row reconstruction (Fig. 4.2), where the on-site potential alternates for every column of the graphene nanoribbon. We call this a grating potential $V_g = V_g^0 + i\Gamma_g$.

The bandstructure of an armchair terminated graphene nanoribbon has a gap at the Fermi energy and the two Dirac cones of the graphene bandstructure are projected on top of each other (compare with Fig. 4.7).
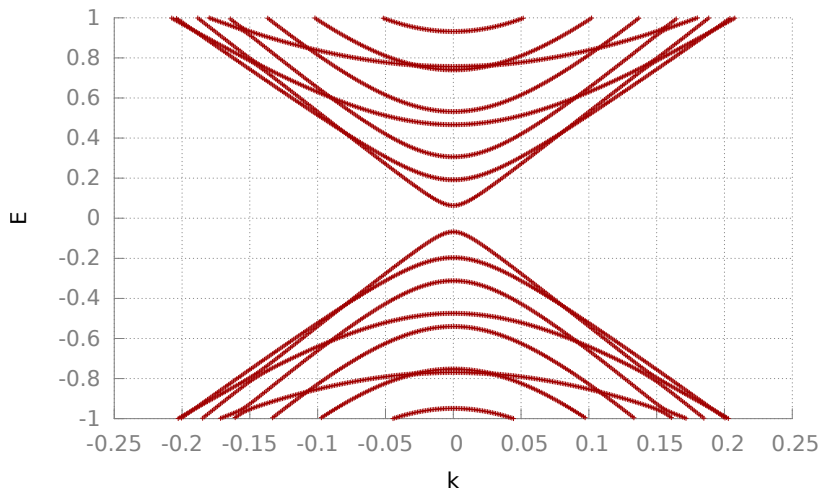

Figure 4.7: Bandstructure for an armchair nanoribbon with a width of 102 atoms. (same as Fig. 3.8)

If we fix the energy E_F inside the gap in the absence of a potential ($V_0 = V_g = 0$), then the k-value for the first state (marked in Fig. 4.8) will be completely imaginary (with $\text{Re}(k) = 0$, blue dots in Fig. 4.8). When a grating potential V_g is introduced, the bandstructure shifts to higher (or lower) k-values. At some point, V_g^0 is large enough that the fixed energy is no longer inside the gap (blue triangles or squares in Fig. 4.8). The spectrum becomes completely real. This behavior corresponds to the square root of a real number, which is zero at around $V_c^{\text{EP}} = (0.2900505 \pm 0.0000005) + i0.0$. This point is an exceptional point.
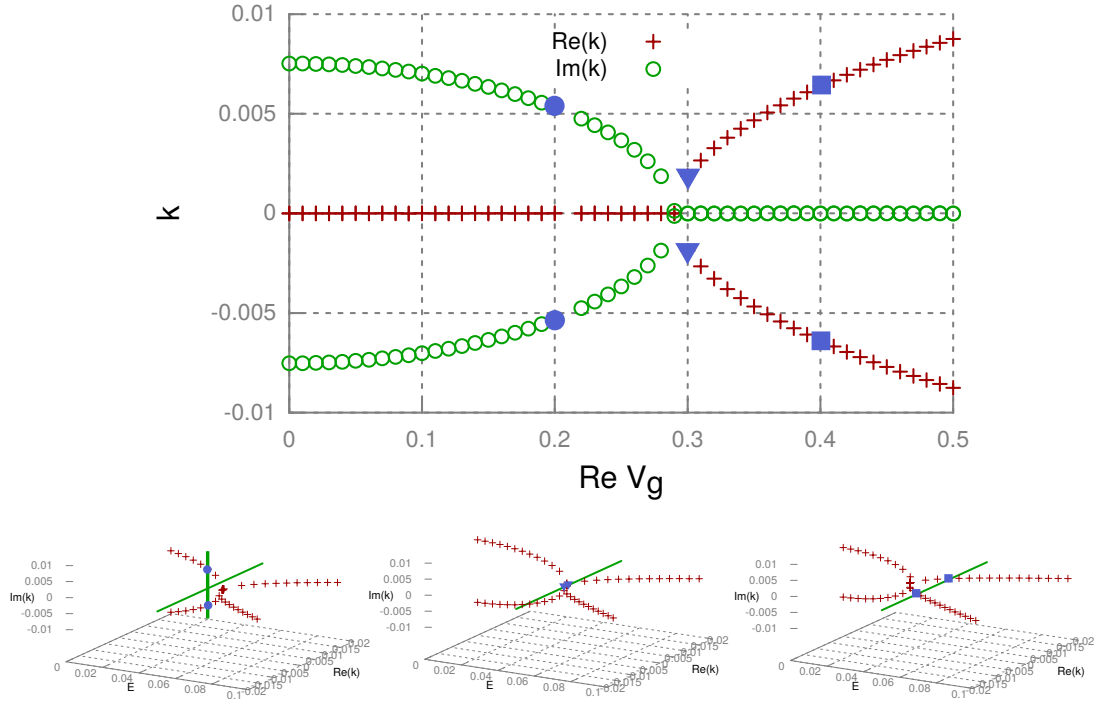
Figure 4.8: Behaviour of the modes around the EP. The *top panel* shows a cut through the Riemann surface at $\mathrm{Im}(V_g) = 0.0$. The red crosses (green circles) denote the real part (imaginary part) of the crystal momentum k. The blue symbols correspond to the blue symbols in the lower three panels. The *lower three panels* show a zoom of the inverse bandstructure, increasing the real grating potential from left to right. The energy is fixed at $E = 0.05$, marked by a green line. The blue symbols in the lower panels indicate the point where the green line intersects with the band. We mark the same V_g values with blue symbols in the upper panel.

In order to find Riemann surfaces that resemble the one shown in Fig. 2.2, a second parameter has to be varied. Following the argumentation in the last section this can either be the tunneling probability $\mathrm{Im}(V_g) = \Gamma_g$ or the hopping parameter t. Figure 4.9 shows the resulting plot for variation in the $\mathrm{Re}(V_g)$-$\mathrm{Im}(V_g)$-plane.
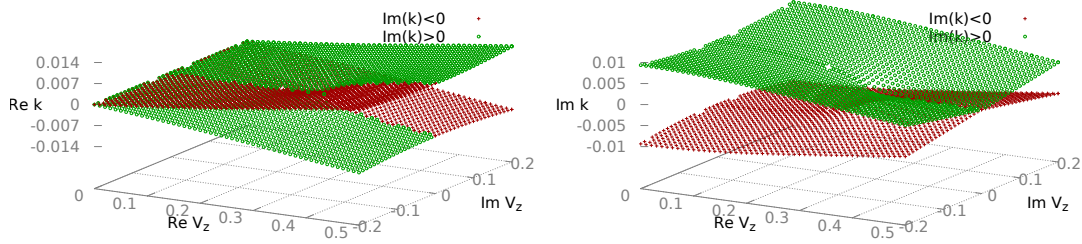
Figure 4.9: Riemann surface for a $w \approx 102\text{Å}$ wide graphene nanoribbon, at $E = 0.05$ for grating potential V_g varied in the complex plane. The EP is at $V_g = (0.2900505 \pm 0.0000005) + i0.0$. The color coding represents the sign of the imaginary part. *Left panel:* Real part of the k-eigenvalue. *Right panel:* Imaginary part of the k-eigenvalue.

It is important to identify the coupled states in this example. The lower row in Fig. 4.8 shows that it is the "upper" and "lower" branch of one state in a $k(E)$ plot. This corresponds to the "left" (negative slope) or "right" (positive slope) branch of one state in the $E(k)$ plot (Fig. 4.7), representing a wave that propagates through the nanoribbon either to the left or to the right[5]. This will restrict the possibilities when investigating the dynamics around the EP, on which we discuss in chapter 5.

The armchair Riemann surface has another interesting feature, represented in Fig. 4.10. There are multiple exceptional points. They are all situated on the real axis and the spacing decreases for increasing $\text{Re}(V_g)$. This will be relevant when we discuss dynamics.

For all the plots presented above, the varied external parameters were the real and imaginary part of the sublattice splitting potential. As discussed before, varying the hopping parameter t is also an option. Starting from Fig. 4.8 we need to introduce a small Γ, to make the Hamiltonian non-hermitian. Variation in t yields the Riemann surface plotted in Fig. 4.11. Please note that this is done only by modulating the nearest neighbor hopping parameter t_1. For a $w = 102\text{Å}$ wide armchair ribbon with the energy fixed at $E = 0.05$ and the imaginary part of the grating potential $V_g = 0.01$ the exceptional point is located at $\text{Re}(V_g)_{\text{EP}} = 0.0, t_{\text{EP}} = 0.874125 \pm 0.000025$. This shows clearly that in accordance with Eq. (4.1) we can also calculate a Riemann surface and, thereby, find an EP when varying the real part of the grating potential and the hopping parameter. We leave this statement as is and focus on the variation of other external parameters. This is because we interpret the modulation of the hopping parameter as a change in bond length (i.e. strain), which would be accompanied by a modulation of the higher order hoppings and be constrained to realistic strain patterns. Two restrictions which were neglected at this point.

---

[5]This interpretation is easily explained by considering the group velocity $v_G \propto \frac{\partial E}{\partial k}$.
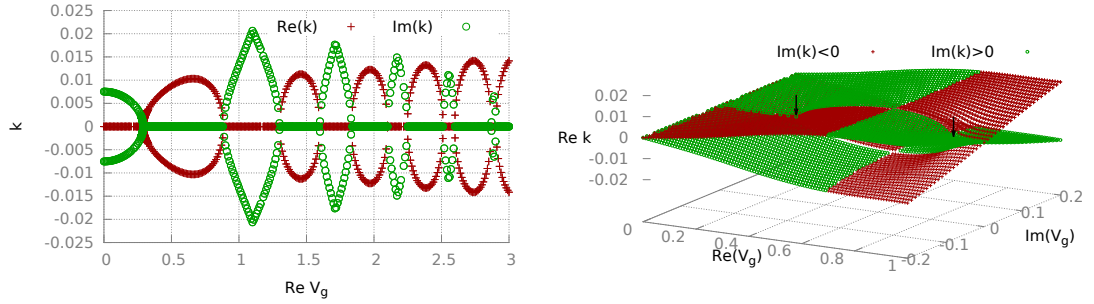
Figure 4.10: A graphene nanoribbon shows more than one EP in the complex V_g plane. *Left panel:* Cut through the Riemann surface at $\mathrm{Im}(V_g) = 0.0$. All points where both the real (red crosses) and the imaginary (green circles) part of k vanish are EPs. *Right panel:* Riemann surface around the two EPs (arrows). Real part of the eigenvalues color coded according to the sign of the imaginary part (red equals positive and green equals negative $\mathrm{Im}(k)$) of the respective eigenvalue. Note how the color coding indicates a certain kind of "mirror symmertry" between adjacent EPs.
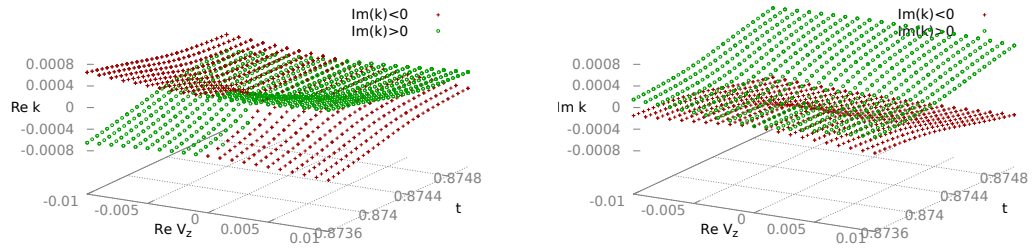

Figure 4.11: Riemann surface for a $w = 102\text{Å}$ wide armchair ribbon with $E = 0.05$ and $V_g = 0.01$. We find the EP on the t-axis at $t_{\mathrm{EP}} = 0.874125 \pm 0.000025$. The color coding corresponds to the sign of the imaginary part of the respective eigenvalue. *Left panel:* Real part of the eigenvalues. *Right panel:* Imaginary part of the eigenvalues.

4.3.2 Non-generic armchair with grating potential

While the exceptional point presented above occurs generically in every armchair termi-
nated graphene nanoribbon, there are other EPs, that only occur for a specific ribbon-
width and energy. Figure 4.12 illustrates how two modes that are (truly) degenerate
begin to couple and exhibit a nonzero imaginary k-value for imaginary V_g. This seems to
happen for all real crossings (as opposed to avoided crossing), although the magnitude
of the imaginary part of k varies considerably from crossing to crossing.
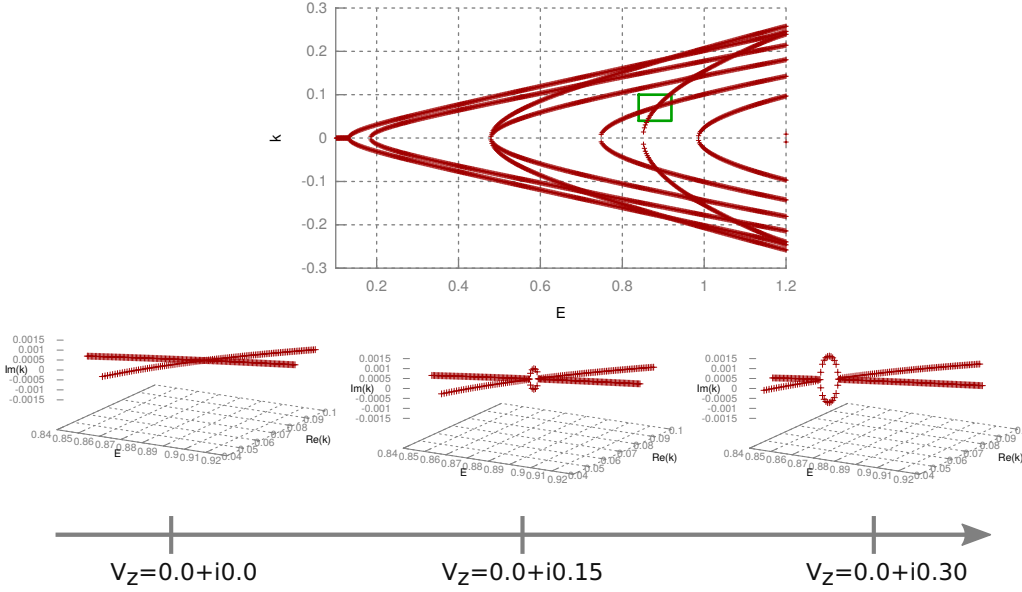

Figure 4.12: *Top panel:* Inverse bandstructure of a $w = 48$Å wide armchair ribbon. The
green rectangle marks the real crossing that we track in order to find a
non generic EP. *Lower panels:* Zoom in to the real crossing in the green
rectangle in the upper panel showing the behavior of the eigenvalues at the
crossing as a function of an imaginary grating potential V_g.

By fixing an energy near a crossing and tracking the evolution of the crystal momentum
k as a function of V_g we can draw a Riemann surface as shown in Fig. 4.13. Although
this kind of exceptional point does not occur generically, it has the advantage of coupling
two modes with a finite group velocity of the same sign. For the EP presented previously
the two modes that couple have group velocities of opposite sign, which makes the group
velocity at the EP zero, which will be a problem when trying to exploit the dynamics
around an EP in a transport experiment.

The inverse bandstructure in Fig. 4.12 also contains many avoided crossings. The
phenomenon shown in the lower row of Fig. 4.12 does not happen there, in other words,
two states that have an avoided crossing at a certain energy do not have an EP at that
energy. We do not have a satisfying explanation why real and avoided crossings act
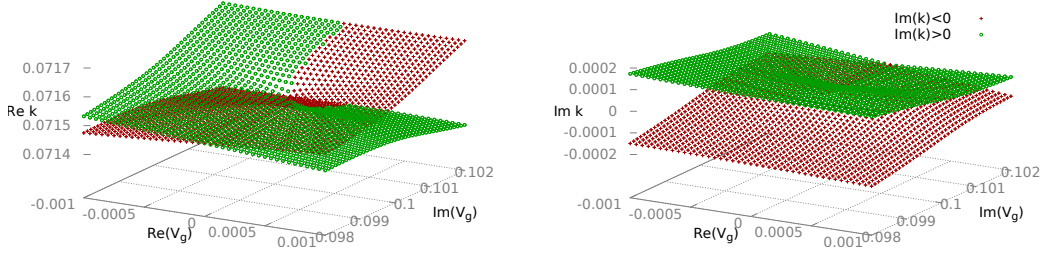so differently. However, the behavior of the modes around an avoided crossing when

Figure 4.13: Eigenvalue spectrum of the fifth and sixth mode of a $w \approx 48\text{Å}$ wide armchair nanoribbon, for an energy fixed at $E = 0.882883$. The varied parameters are the real and imaginary part of the grating potential V_g. There is an EP at $V_g^{EP} \approx 0.0 + i0.1003$. The color coding represents the sign of the imaginary part, red (green) for a state that experiences gain (loss). *Left panel:* Real part of the eigenvalues. *Right panel:* Imaginary part of the eigenvalues.

turning on an imaginary potential is very different to what we see at real crossings and might be worthwhile to study. We do not include this here due to the limited scope of this thesis.

Avoided crossings are degeneracies lifted by an interaction and have been described as early as 1929 by Wigner and von Neumann [43]. Such an interaction is forbidden for the two states we investigate (see Fig. 4.12 and 4.13) due to their odd and even symmetry.

4.3.3 Zigzag with a sublattice splitting potential

In this section we discuss a zigzag ribbon with a complex sublattice splitting potential, for instance a ribbon placed on hexagonal boron nitride. As already discussed, the zigzag-ribbon has a topologically protected edge state and, hence, does not have a gap. We, however, focus on the 1st "normal" state, marked in Fig. 4.14. This is necessary because the only EP for the zigzag ribbon are generic ones that couple two modes propagating in opposite directions, which is not possible for the edge state. Also, for the zigzag ribbon the two Dirac cones are not superimposed, hence, there are no other crossings that could feature an exceptional point.

This discussion is also valid for generic EPs for a complex sublattice splitting potential in armchair graphene nanoribbons. Because the analysis would be practically identical for the armchair ribbon we omit it.

Figure 4.15 shows the Riemann surface for a zigzag ribbon that is $w = 58\text{Å}$ wide at zero energy but with a constant potential of $V_0 = -0.1$. At $V_z = 0.0 + i0.0$ the fixed energy $E = 0.0$ is inside the gap and the k-values for the two states have a finite imaginary part of opposite sign. Complementary to the exceptional point for an armchair ribbon (see Fig. 4.9) the EP is located on the imaginary axis, at $V_z^{\text{EP}} = 0.0 + i0.255$.
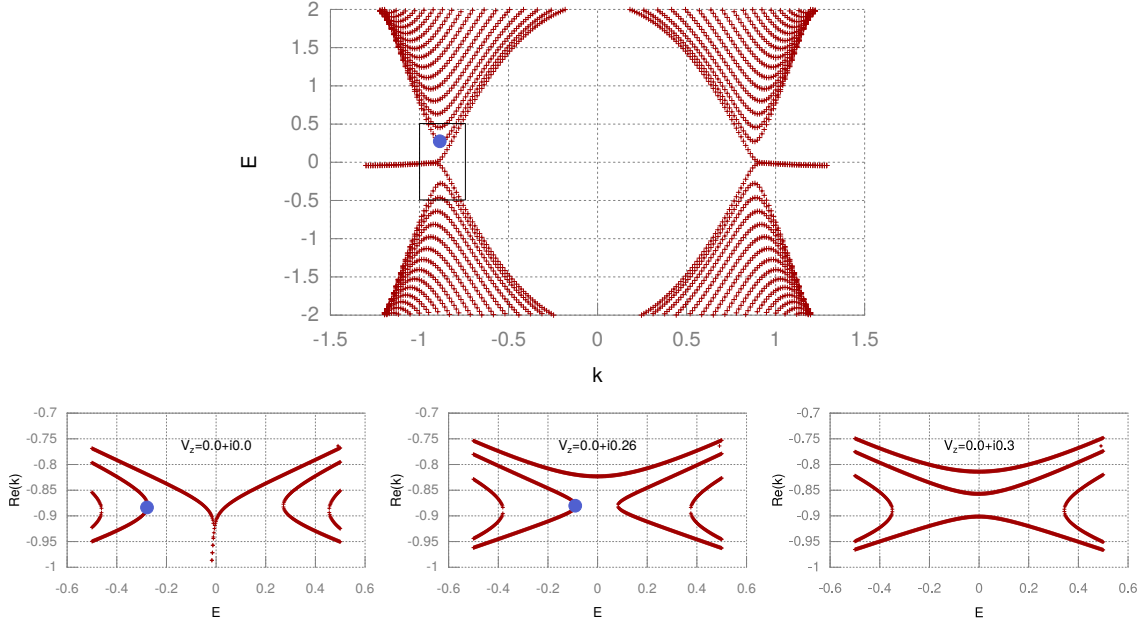
Figure 4.14: *Upper panel:* Bandstructure $E(k)$ for a $w \approx 85$Å wide zigzag nanoribbon without a potential. The spectrum is always gapless due to a topologically protected edge state. The blue dot marks the mode for which we show the EP in Fig. 4.15. *Lower panels:* Real part of the inverse bandstructure $k(E)$ around $E = 0.0$, the blue dot denotes the same state as in the upper panel. Inside the gap the crystal momentum is imaginary. As we increase the imaginary part of the potential $\text{Im}(V_z)$ from left to right, the gap closes. For a certain potential the gap vanishes and the k-eigenvalues are completely real. We find a generic EP for any energy inside the gap. Compare this with the behavior of infinite graphene in Fig. 3.5.
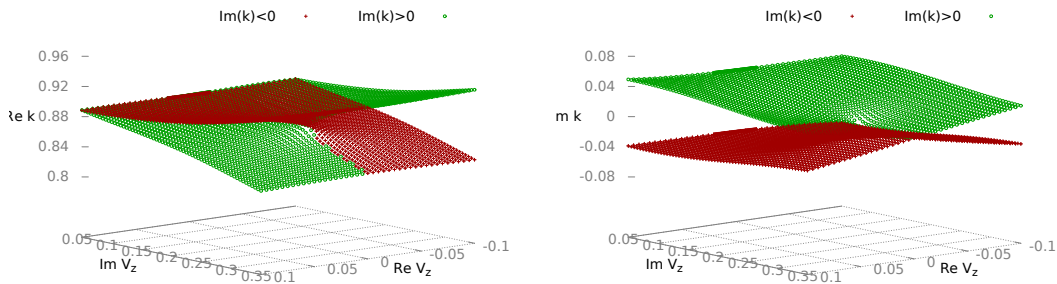

Figure 4.15: Eigenvalue surface for a $w \approx 85$Å wide zigzag nanoribbon at $E = 0.1$. We vary the real and imaginary part of the sublattice splitting potential V_z and find an EP at $V_z^{\text{EP}} = 0.0 + i0.255$. The color coding represents the sign of the imaginary part, red (green) for a state that experiences gain (loss).

4.3.4 Parity-Time symmetry

For all Hamiltonians examined in this chapter so far V_0 in Eq. (3.13) was purely real. This implies that they all commutate[6] with the parity-time operator $\mathcal{PT}$. The $\mathcal{PT}$-operator has only real eigenvalues, hence, because they commute and therefore have a common set of eigenvectors, the energy eigenvalues are real. In non-hermitian physics exceptional points are associated with a spontaneous breaking of this symmetry [2, 12]. This provides a nice interpretation for the EP in an armchair ribbon as (for example) shown in Fig. 4.8. For values $\Gamma = 0, V_z^0 \gtrsim 0.29$ the eigenvalues are real, for lower values of V_z^0 they are complex, making $V_z = 0.029 + i0.0$ an exceptional point.

We also investigated systems without $\mathcal{PT}$-symmetry, by lifting the balance between gain and loss by adding a complex V_0. Figure 4.16 shows such a Riemann surface, calculated for a $w = 61\text{Å}$ wide armchair ribbon with $V_0 = 0.1i$ and fixed energy at $E = 0.05$. The EP is approximately at $V_g^{\text{EP}} = (0.5915 \pm 0.00025) + i(0.525 \pm 0.001)$.
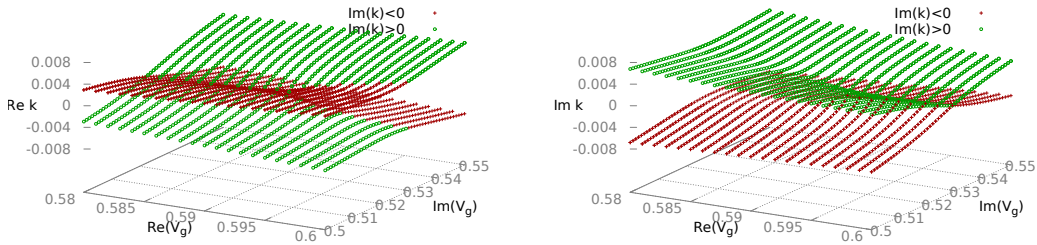

Figure 4.16: Eigenvalue spectrum as a function of a complex grating potential V_g for a $w = 61\text{Å}$ wide armchair ribbon with $V_0 = 0.1i$ and the energy fixed at $E = 0.05$. The EP has moved away from the real axis and is approximately at $V_g^{\text{EP}} \approx 0.5915 + i0.525$. A red (green) color coding shows a negative (positive) sign of the imaginary part of the eigenvalue. *Left panel:* Real part of the eigenvalue spectrum. *Right panel:* Imaginary part of the eigenvalues.

The most prominent effect we observe is that the EP has moved away from the real (or imaginary) axis[7]. The deviation of the position of the EP with respect to its position for a $\mathcal{PT}$-symmetric Hamiltonian $|\Delta V_z| = |V_{z\text{EP}} - V_{z\text{EP}}^{\mathcal{PT}}|$ is always larger than the complex V_0 that lifts $\mathcal{PT}$-symmetry, $|\Delta V_z| \geq |V_0|$. This is shown in Fig. 4.17, where the red crosses with errorbars mark the positions of the EP for stepwise increasing PT-symmetry breaking potential V_0 (green circles). For $V_0 > 0.04$ the position of the EP on the imaginary axis grows approximately linear. Therefore, we numerically verified the statement that in terms of the experiment an EP only occurs if there is periodic gain and loss, respectively, present in the nanoribbon. To realize this requirement, we need to modify the device proposed in Fig. 4.1 by adding an extra insulating plus conducting layer as shown in Fig. 4.18.

---

[6] $[H, \mathcal{PT}] = 0$

[7] The symmetry of the Riemann surface w.r.t. the axes is a consequence of PT-symmetry.
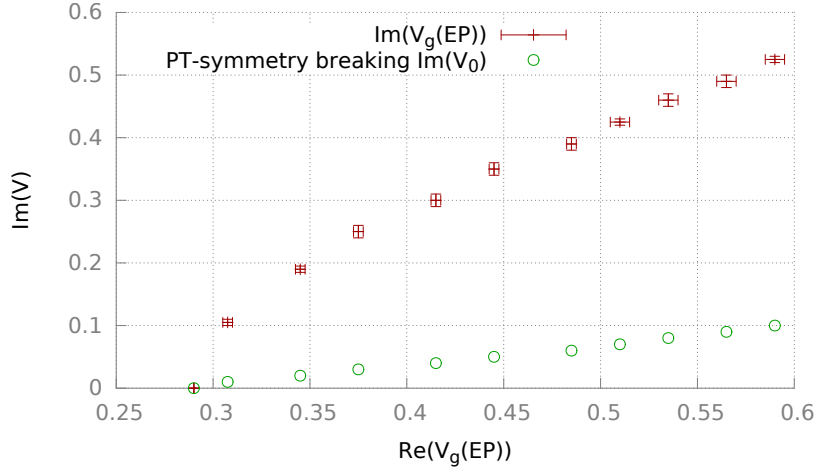
Figure 4.17: Position of the generic EP of a $w = 61\text{Å}$ wide armchair ribbon in the complex V_g plane (red crosses with error bars) for a stepwise increasing gain-loss-balance breaking potential $\text{Im}(V_0)$ (green circles). The stepwidth is $\Delta\text{Im}(V_0) = 0.01$. For $\text{Im}(V_0) > 0.04$ the imaginary potential at the EP $\text{Im}(V_g^{\text{EP}})$ grows linearly, and, hence, will always remain larger than $\text{Im}(V_0)$. We verified this for the entire relevant potential window (not shown).
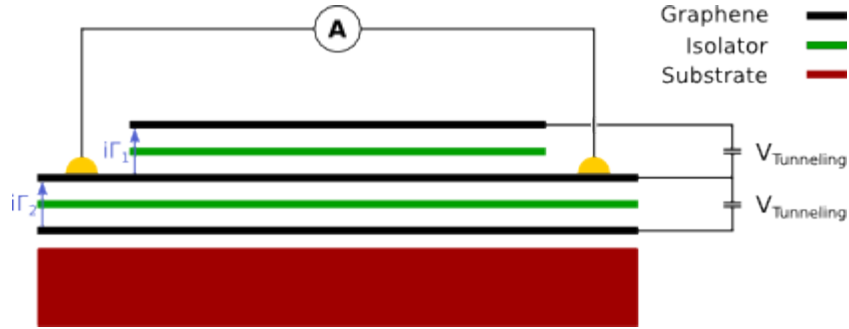

Figure 4.18: Sketch of the adapted device. Three graphene flakes (black) are separated by a single or a few layers of an insulator. The graphene flakes will be connected by tunneling rates Γ which can be controlled by varying the number of insulating atom-layers or tuning the tunneling voltage $V_{tunneling}$. Measuring the conductivity for the middle flake yields information on the transmission probability.

This hypothetical device consists of a graphene layer encapsulated between two hBN monolayers, with conductors on the top and bottom. The tunneling voltage between the graphene and the two conductors can be modified in such a way that the tunneling rate Γ_1 to the graphene flake is the same as the tunneling rate Γ_2 for leaving the flake, corresponding to a $\mathcal{PT}$-symmetric Hamiltonian or de-tuning it to realize a non-$\mathcal{PT}$-symmetric Hamiltonian.

5 Dynamics in the vicinity of exceptional points

After revealing the existence and location of exceptional points in graphene we want to investigate dynamics in their presence. Inspired by the experiments demonstrating dynamical encircling of an EP (as described in Sec. 2.3) we focus on transport through nanoribbons with longitudinally changing parameters. This section presents the results found, focusing on the $\mathcal{PT}$-symmetric case where gain and loss is balanced, because as mentioned before, all of our results point towards the conclusion, that there are no EPs if there is not alternating gain and loss.

We will start with the discussion of armchair ribbons with a grating potential because it is a very instructive case. The armchair ribbon has two kinds of EPs, the first occuring generically and the second appearing only at certain crossings. In the end we will discuss a zigzag ribbon with a sublattice dependent potential.

All the energies and potentials in this chapter are given in electron volt. We omit them for clarity.

5.1 Physical motivation

We map the adiabatic evolution of a state in time to a longitudinal parameter variation along a graphene nanoribbon. Hence, instead of a time resolved scattering experiment, we simulate a transport experiment. Applying a finite bias to the nanoribbon leads to a current that can be measured to calculate the conductivity $G = I/U$. We describe this theoretically by considering scattering through a finite structure with (semi-)infinite leads, where we fix the energy E of the incoming electrons. We can assign numbers to the modes in the leads and then calculate the transmission t_{ij} from a certain mode j in the incoming lead to a mode i in the outgoing lead. The insertion energy is proportional to the bias applied to the nanostructure and the macroscopic conduction G can be calculated by multiplying the total transmission $T = \sum_{ij} t_{ij}$ with the electronic flux quantum: $G = T\frac{e^2}{h}$.

While earlier we considered bandstructures and, hence, infinite nanoribbons for a uniform potential $V = V^0 + i\Gamma$, we now consider a locally varying $V = V(\vec{r}) = V^0(\vec{r}) + i\Gamma(\vec{r})$. For instance hexagonal boron nitride (hBN) and graphene have a lattice mismatch of 1.8% which results in a so called moiré structure (Fig. 4.2). There, the stacking configurations change on a scale which is proportional to the inverse of the lattice mismatch. Hence, the on-site potential V_z^0 and the tunneling rate Γ change on the same scale.

With these remarks we can motivate the change of V_z along a graphene nanoribbon assuming hBN is used as substrate and insulating layer. Note, however, that this is only a motivation and we do not provide a realistic set of parameters, because the ab-initio simulation of tunneling probabilities in graphene on hBN goes beyond the scope of this thesis. For the armchair ribbons we consider a grating potential V_g that alternates for every other row of carbon atoms along the ribbon. This corresponds to the ribbon being placed on a reconstructed surface.

In this first study we restrict ourselves to perfect graphene nanoribbons. Investigating ribbons with defects or imperfect edges was beyond the scope of this thesis. Because of their very different bandstructure we discuss the zigzag- and armchair-nanoribbons separately.

5.2 Armchair with grating potential – a generic EP

For a $w \approx 61$Å wide ribbon we fix the energy at $E = 0.05$ inside the gap and find a Riemann surface as shown in Fig. 5.1. The EPs are located on the Re(V_g)-axis, situated at $V_g = (0.2900505 \pm 0.0000005) + i0.0$ and mirrored across the imaginary axis at $V_g = (-0.2900505 \pm 0.0000005) + i0.0$. A real crossing connects them[1].
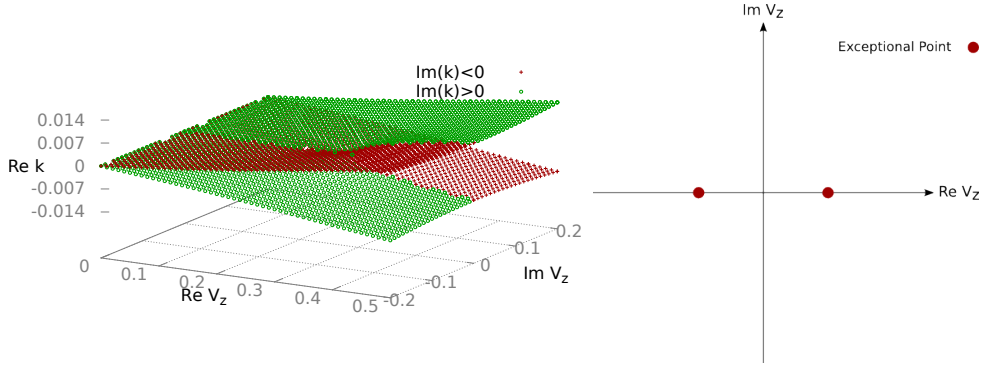
Figure 5.1: *Left panel:* Real part of the eigenvalues of the investigated graphene nanorib-
bon for variable grating potential V_g. The ribbon is $w \approx 61$Å wide, the energy
is fixed at $E = 0.05$ and we find an EP at $V_g \approx 0.290 + i0.0$. The color cod-
ing shows the sign of the imaginary part, red (green) corresponding to gain
(loss). *Right panel:* Position of the EPs (red dots) in the complex V_g-plane.

We investigate transport by imagining devices where the values of Re(V_g) and Im(V_g) change adiabatically when going along the x-direction of the device (compare with previous section). Such a parameter variation along the x-direction is shown in Fig. 5.2 on the left panel. The parameter variation as a function of x can be interpreted as a path in the Re(V_g)-Im(V_g)-plane (right panel in Fig. 5.2). Usually, we choose this path to be circular or elliptical. Due to technical limitations this path has to start on the Re(V_g)-axis[2].

For a device that represents such a parameter-variation we calculate the transmission T from left to right and the transmission T' from right to left. The same goes for R and R'. Wherever it is necessary to distinguish, we will call the transmission (reflection) for a positive tunneling voltage T_+ (R_+), for negative tunneling voltage T_- (R_-) and without tunneling T_0 (R_0).

---

[1]This follows from the energy being fixed inside the gap, the eigenvalue at $V_g = 0.0 + i0.0$ has to be purely imaginary.

[2]The tight-binding solver we use [44] requires a real potential for the semi-infinite leads.
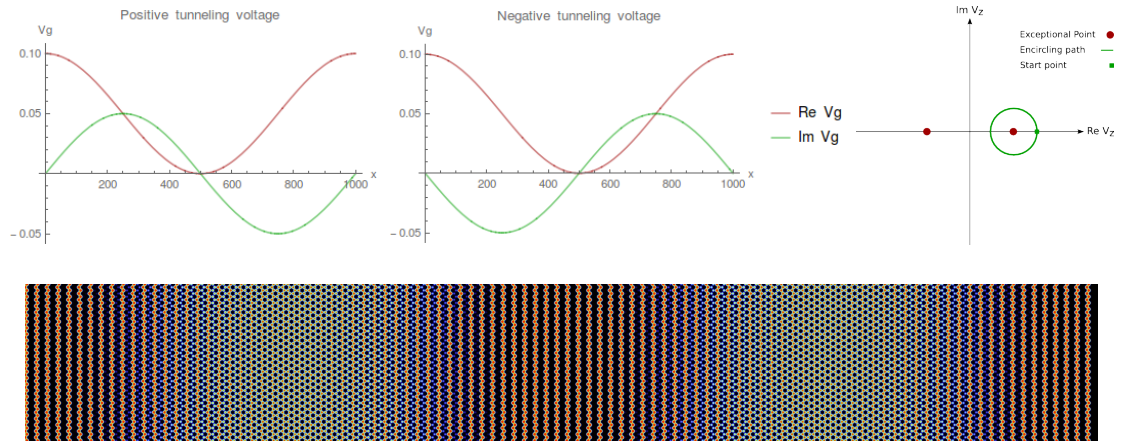
Figure 5.2: *Upper left and center panel:* Local sublattice-splitting potentials $V_g^0(x) = \mathrm{Re}(V_g(x))$ and $\Gamma(x) = \mathrm{Im}(V_g(x))$ as a function of the position along the ribbon. *Upper right panel:* Path in the complex V_g plane. *Lower panel:* Real part of the grating potential along a short ribbon. The color scale ranges from black (minimum) to red (maximum), same as in Fig. 5.14.

For this EP the two modes that couple are the left- and right-going mode. Hence, when measuring the conductance there is only one mode accessible. Following the remarks in section 2.3 we naïvely expect transmission to be large for one mode and the other mode to be suppressed and inverse when passing through the parameter path in the opposite direction, i.e. when passing through the ribbon in the opposite direction. In other words, the same mode that is transmitted well in the first direction will be suppressed in the other. Hence, we expect to observe a diode-like transmission.

5.2.1 EP centered circular paths

In a first step we consider a circular path centered around the EP. As Schumer reports [7], not all radii show chirality, therefore, we vary the radius of the parameter-circle. Transmission vs. radius is plotted in Fig. 5.3. T_+ corresponds to a positive tunneling voltage and T_- corresponds to a negative tunneling voltage. Apparently, the real potential dominates the transmission behavior, as there is little to no difference to the transmission with the same real potential without imaginary part (labeled T_0 in Fig. 5.3). This behavior is connected to the existence of a gap. When adiabatically moving along the circular path the electron moves through an area with no local density of states (e.g. at $V_g^{\mathrm{EP}} - r_{V_g}$). This will become more clear with the next example.

The behavior when encircling the EP is vastly different from what we expected because the ribbon is Lorentz reciprocal [45]. Lorentz reciprocity is a property from electromagnetism that requires the scattering matrix that connects the incoming and outgoing currents to be symmetric (for details we refer the reader to [45]). For the nanoribbons presented in this thesis this implies[3] $T = T'$.

---

[3]Even though reciprocity is not broken it can be circumvented for individual modes when there are
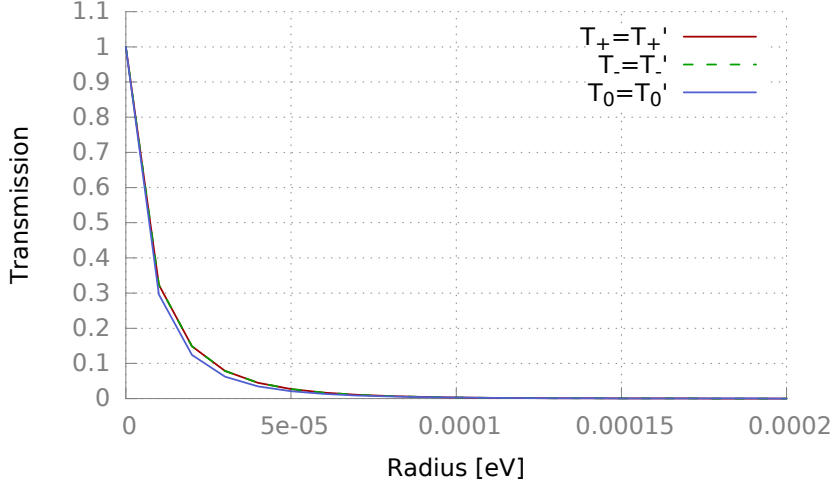
Figure 5.3: Transmission for a parameter variation that describes a circular path in the complex V_g plane, centered around the EP. T_+, T_- and T_0 denote the transmission for a positive, negative and no tunneling voltage, the primed quantities indicate transmission from the other direction. Apparently the real potential dominates, because the transmissions with imaginary potential (T_+, T_-) do not deviate from the transmission for a real potential T_0.

The reflections for incoming modes from the left side R and from the other side R' are not required to be equal. Two electrons that are transmitted through the structure in opposite directions will experience no net gain or loss because they pass through all the parts of the structure with positive and negative imaginary potential. An electron that is reflected does not probe the full structure but only part of it, hence, it can experience net gain or loss. This is manifested in Fig. 5.4, where for the real potential the reflection R_0 goes towards zero (fulfilling the condition $T_0 + R_0 = 1$), while the left reflection R and the right reflection R' are not equal and do not sum up to one with the transmission ($T + R \neq 1$) due to the absorbing/emitting potential.

---

several of them present. Because the transmission is defined as $T = \sum t_{ij}$ and $T' = \sum t_{ji}$, it is still possible to find $t_{ij} \neq t_{ji}$.

Comparing the transmission for positive (T_+), negative (T_-) and hermitian (T_0) dynamics yields almost identical results (see Fig. 5.3). We conclude that the imaginary potential does not influence the transport properties, and therefore no chiral behavior emerges.
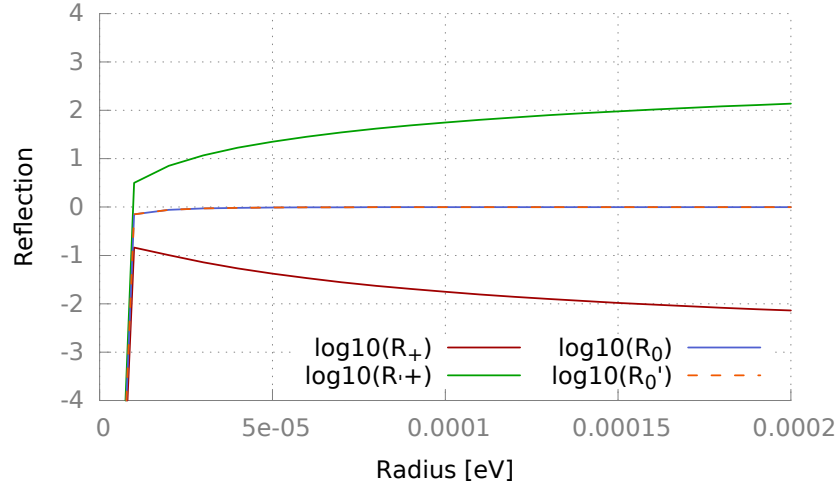

Figure 5.4: Reflection for a parameter variation that describes a circular path in the complex V_g plane, centered around the EP. R_+ and R_0 denote the reflection for a positive and no tunneling voltage, respectively. The primed quantities indicate reflection from the other direction. Please note the logarithmic scale! For $r = 0$, i.e. no parameter variation, all reflections are zero. While for a finite radius R_0 and R_0' quickly go to one, the reflection with imaginary potential is amplified for one side R_+ and damped for the other R_+'. This is reversed for negative tunneling voltage (R_- and R_-', not shown for clarity.)

5.2.2 Circular paths with variable center

While we do not find interesting behavior when encircling the EP, another category of quasi-adiabatic paths can be investigated by fixing the radius of the path and moving its center along the real axis. This experiment shows whether containing the EP inside the circle actually has an effect on the transmission properties. Figure 5.5 shows, that T is effectively zero up until a critical value $V^0_{zcenter} \approx 0.4$, which corresponds to $V^0_{zcenter} = V_{z\mathrm{EP}} + 2r$, with the radius of the parameter-circle $r = 0.05$. For smaller values of $V^0_{zcenter}$ transmission is blocked because the local density of states at E_F vanishes in some areas along the ribbon.
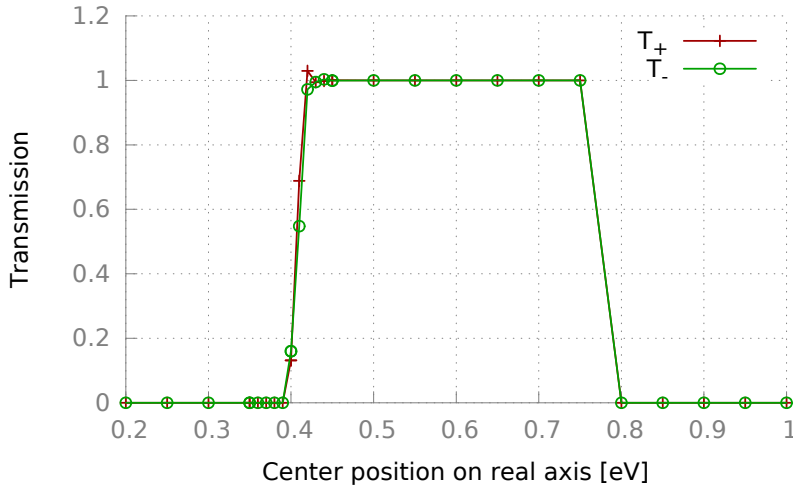

Figure 5.5: Transmission of a $l = 42000\text{Å}$ long nanoribbon, where the potential passes through a circular path of $r = 0.05$ in the complex V_g plane. The center is moved along the real axis and the transmission is recorded for a given center position. The ribbon is $w = 61\text{Å}$ wide. Evidently, the transmission is zero for $V^0_{zcenter} < V_{z\mathrm{EP}} + r$, and unity for larger values. We associate this with the state having to tunnel through a region of zero density of states, where it will be exponentially suppressed.

At approx $V^0_{zcenter} \approx 0.4 \approx V_{z\mathrm{EP}} + 2r$ transmission is equal to one. This is interesting, because it is exactly what we expect for adiabatically changing the parameters in a hermitian system. Apparently, the adiabatic theorem holds although the electron passes through an imaginary potential. Another surprising feature is that the transmission drops again to zero at about $V_{zcenter} = 0.77$. Comparing this behavior with Fig. 4.10 reveals that this drop is connected to a second EP. This is highlighted in Fig. 5.6 by overlaying Fig. 4.10 with a cut through the Riemann surface at $\mathrm{Im}(V_z) = 0$. Continuously shifting the center of the parameter path repeats the same pattern for multiple EPs, in line with the Riemann surface presented in Fig. 4.10.
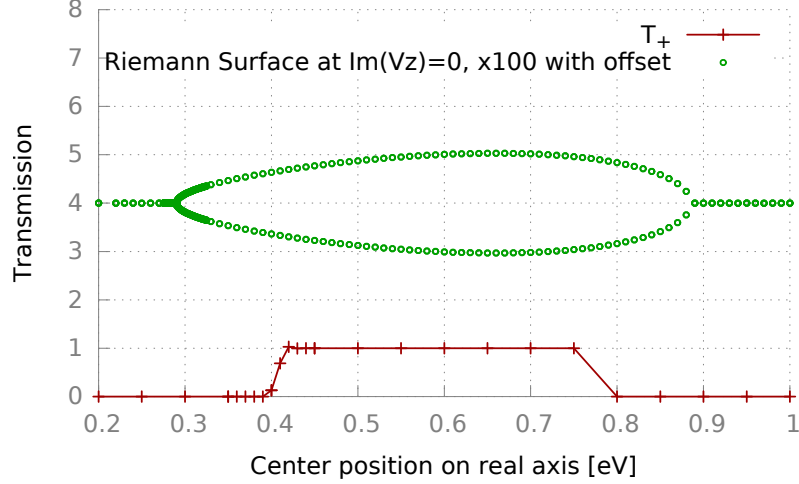
Figure 5.6: Same figure as above (Fig. 5.5), with a linecut through the real Riemann surface $\text{Re}(k(V_g))$ at $\text{Im}(V_g) = 0.0$. The figure illustrates that the transmission is zero when the electron passes through a parameter region were $\text{Re}(k) = 0$.

When the center (in Fig. 5.5) is at approximately $V_g \approx 0.4$ the transmission T_+ is briefly larger than one, whereas T_- does not seem to exceed one. We investigate this small difference between T_+ and T_- by either omitting by the imaginary potential or by increasing the length of the ribbon (Fig. 5.7). Without an imaginary potential the transmission goes quickly to unity at $V_{gcenter}^0 = V_{g\text{EP}} + r \approx 0.34$. This agrees with the explanation that the transmission alternating between zero and one is actually not linked to non-hermitian physics. The best explanation is that in the areas where the transmission is small, the electrons have to pass through a region with vanishing density of states and, hence, transmission is suppressed if this area is too large. However, we see that the transmission is enhanced at about $V_{gcenter} \approx 0.37$, which is clearly a consequence of the non-hermitian nature of the Hamiltonian. Apparently the difference between T_+ and T_- in Fig. 5.3 is a numerical artifact. If the ribbon is longer, i.e. the parameter variation happens slower, numerical errors seem to dominate, as the transmission fluctuates wildly, but however, clearly exceeds unity. Numerical simulations in non-hermitian physics are prone to numerical errors, especially for large non-hermitian potentials or long propagation in the non-hermitian potential. The exponential nature of the time propagator (or, in our case, Bloch's phase) for an imaginary eigenvalue can amplify even tiny numerical errors.

Another way to highlight the non-hermitian effects around $V_{center} = 0.4$ is to study the wavefunctions directly. Figure 5.8 shows the wavefunctions of $l = 4200\text{Å}$ long ribbons with zero and full transmission. The wavefunction of the ribbon without transmission ($T = 0$, $V_{gcenter} = 0.33$, upper panel in Fig. 5.8) goes to zero along the ribbon as we expect, whereas for the other ribbon with transmission $T = 1$ ($V_{gcenter} = 0.39$, lower panel in Fig. 5.8) we find unexpected behavior: the wavefunction drops to zero in the middle of the ribbon and is then 'revived' in the second half of the ribbon. This is clearly
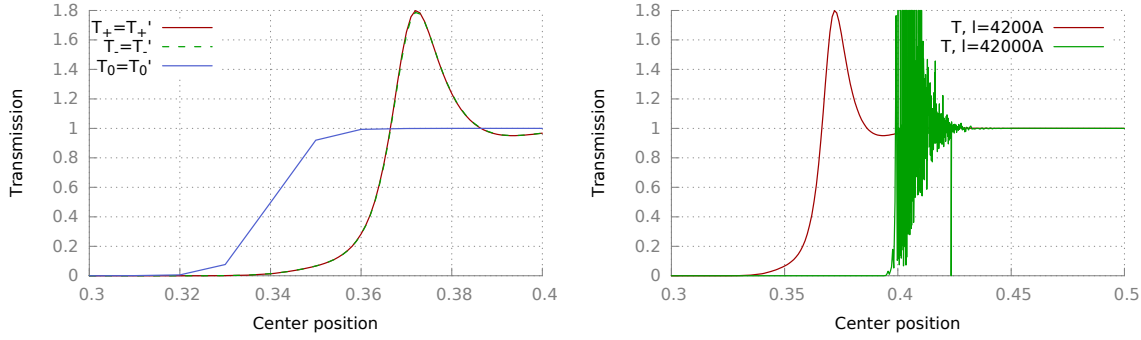
Figure 5.7: Same 'experiment' as in Fig. 5.5, with the area around the onset of transmission enlarged. *Left panel:* Comparison of an oscillation with amplitude $r = 0.05$ of the real potential (blue) around the same center as a circular path in the complex plane with the same radius (red/green) for a $l = 4200$Å long ribbon. The enhanced transmission round $V_g \approx 0.37$ is a feature of the non-hermitian potential. *Right panel:* Comparison of the transmission of a nanoribbon where the potential stretches over $l = 4200$Å (red) and a nanoribbon where the potential stretches over $l = 42000$Å (red). For the long nanoribbon numerical fluctuations seem to dominate in the region of transition from $T = 0$ to $T = 1$.

a non-hermitian effect.

The reflection (left panel of Fig. 5.9) is large for one side while being practically zero for the other one. Again, this is not very surprising, as the wavefunction of a reflected particle mainly probes the first part of the imaginary potential, as seen from its initial direction of motion. If we, however, compare this with the transmission T and transmission phase ϕ_T shown in the left panel of Fig. 5.9, we discover a certain position of the center of the circle where the transmission is one, $T = 1$ and the transmission phase vanishes, $\phi_T = 0$ ($V = 0.386$, vertical black line). This resembles strongly a phenomenon in $\mathcal{PT}$-symmetric optics called "unidirectional invisibility. The expression describes a Bragg grating of optically active materials that are designed to absorb the incoming light from one direction and (re-)emit into the other direction, while being invisible in transmission by having $T = 1$ and a vanishing transmission phase[4] $\phi_T = 0$. This was described and realized recently [46, 47, 48]. Although, at first glance all these criteria are met, for a unidirectional invisible grating these properties hold for a large range of incoming frequencies, which is not true in this case.

---

[4]In this case we define the transmission phase as the phase shift aquired by the electron after passing through the structure. The transmission phase without a potential would also vanish.
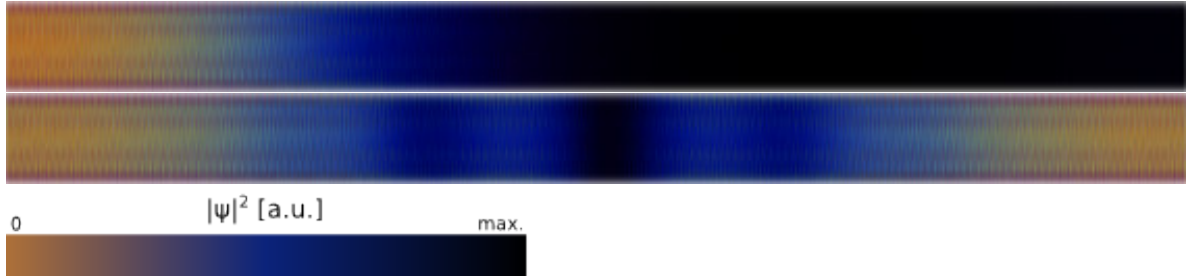
Figure 5.8: Absolute square of the wavefunction $|\psi|^2$ of the ribbon in Fig. 5.5. The aspect ratio of the images do not correspond to the actual $4200\text{Å} \times 61\text{Å}$ ribbons. *Upper image:* Wavefunction for a parameter circle centered around $V_{gcenter} = 0.33$, transmission is $T = 0$. *Lower image:* Wavefunction for a parameter circle centered at $V_{gcenter} = 0.39$ with $T \approx 1$. The wavefunction vanishes in the middle of the ribbon but is 'revived' by non-hermitian effects.
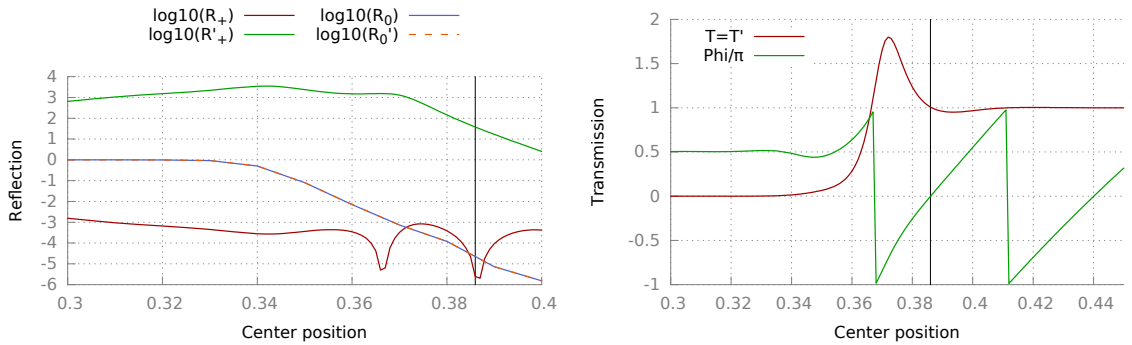

Figure 5.9: Reflectivity and transmission phase for the region of interest around the onset of transmission. *Left panel:* The reflectivity for the hermitian case ($R_0 = R'_0$, blue and orange) is the same for both directions and drops at the onset of transmission according to $T_0 + R_0 = 1$. For the non-hermitian potential the reflectivity is large for one direction R_+ and exponentially small for the other R'_+. The vertical line marks the center position where we find 'unidirectional invisibility'. *Right panel:* The transmission (red) for orientation and the transmission phase (green) divided by π. The vertical black line marks the position where transmission is one and the transmission phase vanishes. Combined with the asymmetric reflectivity this point shows unidirectional invisibility.

5.3 Armchair with grating potential – a non-generic EP

In Sec. 4.3.2 we presented the Riemann surface for an exceptional point that is conceptually different. Although this EP does not occur generically at a known energy and for every ribbon, it has certain advantages. It does not connect two modes that move in opposite directions, but two modes that propagate in the same direction, thus allowing us to observe "chirality" when dynamically encircling the EP. With multiple modes accessible, the "forward" and "backward" transmission from one to another mode can be different, $t_{ij} \neq t_{ji}$, without violating Lorentz reciprocity $T = T'$.

The Riemann surface for a $w = 48$Å wide ribbon is shown in Fig. 5.10, the energy is chosen at $E = 0.882883$ and the two modes connected are the fifth and sixth occuring modes (compare with Fig. 4.12). We find the EP located on the imaginary axis at $V_g^{\text{EP}} = 0.0 + i0.1003$.
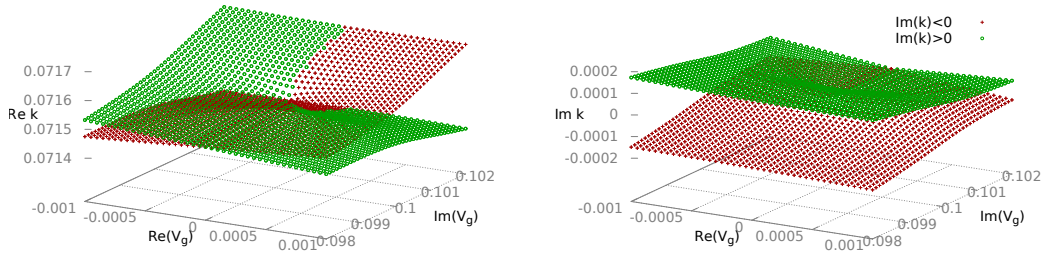

Figure 5.10: Eigenvalue spectrum of the fifth and sixth mode at $E = 0.882883$ for a $w = 48$Å wide armchair nanoribbon. There is an EP in the complex V_g plane at $V_g^{EP} \approx 0.0 + i0.1003$. The color coding represents the sign of the imaginary part, red (green) for a state that experiences gain (loss). *Left panel:* Real part of the eigenvalues. *Right panel:* Imaginary part of the eigenvalues.

5.3.1 EP centered elliptical paths

In a first step we try encircling the EP with an ellipse and vary the semi-axis in the real direction. We do not vary the imaginary semi-axis because we are again technically restricted to start points on the real axis, hence, only one EP-centered radius is possible. The encircling path is shown in Fig. 5.11.

Because there are multiple modes accessible the analysis becomes slightly more involved. We will call the transmission from the incoming mode i to the outgoing mode j t_{ij}. The transmissions t_{ij} can be arranged in a matrix, connecting the modes in the left lead $\psi = (\phi_i, \phi_j)$ to the modes in the right lead $\psi' = (\phi_i', \phi_j')$,

$$
\begin{pmatrix} \phi_i' \\ \phi_j' \end{pmatrix} = \begin{pmatrix} t_{ii} & t_{ij} \\ t_{ji} & t_{jj} \end{pmatrix} \begin{pmatrix} \phi_i \\ \phi_j \end{pmatrix} . \tag{5.1}
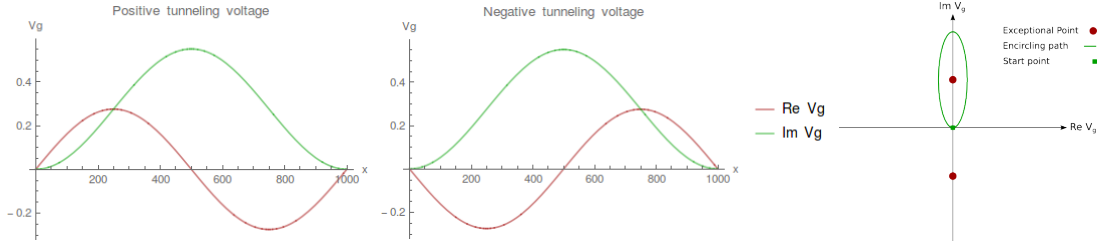$$

Figure 5.11: *Left and center panel:* The local grating potential as a function of the position along the ribbon for positive and negative tunneling voltage. *Right panel:* Parameter path in the complex plane.

The transmissions of interest are t_{55}, t_{56}, t_{65} and t_{66}, and the notation for scattering in the reverse direction is t'_{ij}. First, we calculate them for a $l = 4200\text{Å}$ long ribbon, as shown in Fig. 5.12.
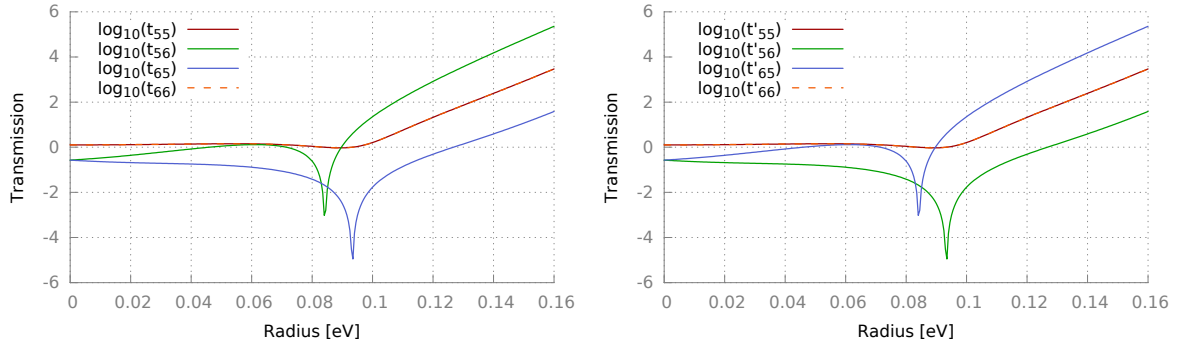

Figure 5.12: Transmission for a $w = 48\text{Å}$ wide and $l = 4200\text{Å}$ long armchair ribbon. The center in the imaginary direction is fixed at the EP $\text{Im}(V_{gcenter}) = 0.1003$ and the radius is equal $r_{im} = 0.1003$ to guarantee a starting point on the real axis. We vary the radius in the real direction r_{re} and find chiral behavior for $r_{re} > 0.09$. How to spot chiral behavior is described in the running text and Tab. 5.1. *Left panel:* Transmission t_{ij} for insertion from the left, i.e. passing counterclockwise through the parameter loop. *Right panel:* Transmission t'_{ij} for insertion from the right, i.e. passing through the loop clockwise.

Apparently for $r > 0.9$ there is chiral behavior in the sense of Sec. 2.3. This can be understood by comparing the orders of magnitude of the various t_{ij} for forward propagation and t'_{ij} for backward propagation. For radii $r > 0.9$ we find[5] $t_{56} > t_{55}$ and $t_{66} > t_{65}$. If we start in mode ϕ_5 we will most likely end up in the other mode ϕ_6, while an electron in mode ϕ_6 will remain in that mode (compare with Tab. 5.1). For the propagation in the opposite direction we find the exactly opposite behavior, hence, encircling the EP yields chiral behavior.

---

[5]In terms of the matrix: one column dominates linewise over the other.

Table 5.1: Exemplary comparison of the orders of magnitude of the transmissions from mode i to j, t_{ij}. The values are similar to $r_{re} \approx 0.1$ in Fig. 5.12.

Counterclockwise		Clockwise	
Start in ϕ_5	Start in ϕ_6	Start in ϕ_6	Start in ϕ_6
$t_{55} \approx 1$	$t_{65} \approx 0.01$	$t'_{55} \approx 1$	$t'_{65} \approx 100$
$t_{56} \approx 100$	$t_{66} \approx 1$	$t'_{56} \approx 0.01$	$t'_{66} \approx 1$
End in ϕ_6	End in ϕ_6	End in ϕ_5	End in ϕ_5
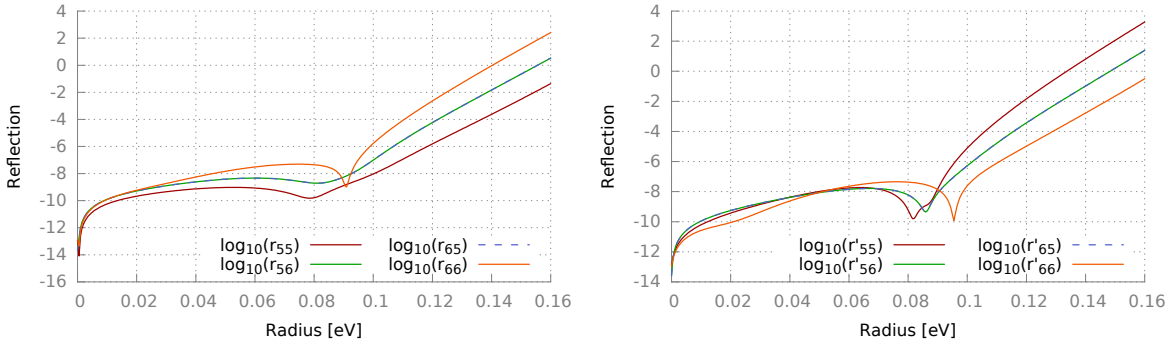
Figure 5.13: For completeness we give the reflection that corresponds to the transmission in Fig. 5.12. *Left panel:* Reflection r_{ij} for insertion from the left, i.e. passing counterclockwise through the parameter loop. *Right panel:* Reflection r'_{ij} for insertion from the right, i.e. passing through the loop clockwise.

A further illustration of the chiral behavior is the change of the wavefunction characteristic after passing through the ribbon. Both outgoing modes have mainly the same characteristics, which we find for the ingoing modes ϕ_5 (see Fig. 5.14).

To make sure that the phenomenon we observe is not just coincidental, we compare with some other modes, for example the first two. As can be seen in Fig. 5.15, the diagonal elements are approximately one, while the off diagonal elements are practically zero. This is exactly what we expect when varying external parameters adiabatically. The electron remains in its instantaneous eigenstate and returns into its initial state after being transported adiabatically along a closed path in parameter space.
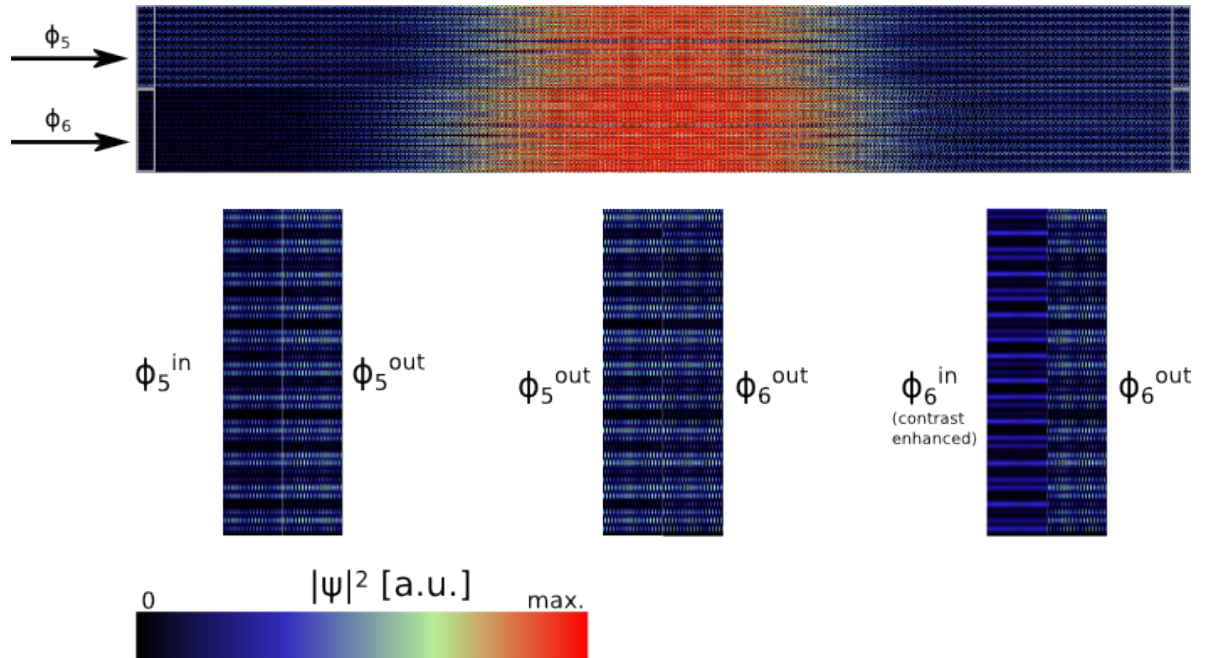
Figure 5.14: Absolute squared wavefunctions $|\psi|^2$ for the ribbon in Fig. 5.12, for $r_{Re} = 0.1$. *Top panels:* Wavefunction for the fifth ϕ_5 and sixth mode ϕ_6 when inserted from the left. Please note that the color scales are not equal because ϕ_6 is amplified disproportionally strong. The grey rectangles mark the areas that are enlarged in the top panels. *Lower panels:* Extracts of the wavefunctions in the lower panels of the incoming and outgoing wave. The enlarged sections are placed next to each other to compare the wavefunction characteristics. The in and outgoing part of ϕ_5 are roughly similar (*left panel*), whereas ϕ_6^{in} and ϕ_6^{out} show very different characteristics (*right panel*). The *middle panel* indicates that the characteristics of the outgoing wave of ϕ_6 are actually those of the incoming wave of ϕ_5. This confirms that irrespective of which mode is inserted, the outgoing mode will be the same.
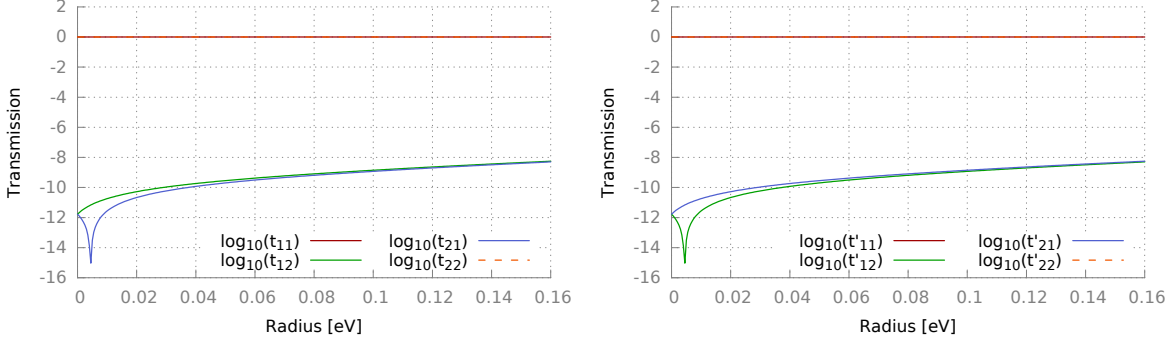
Figure 5.15: Transmissions for the first two modes coming from left and right. The variation of the potential is adiabatically slow, hence, the states are not scattered into each other which can be seen by the diagonal transmissions amounting to one $t_{11} = t_{22} = 1$ and the off-diagonal transmissions being practically zero $t_{12} = t_{21} = 0$.

We want to test whether chirality is also present for longer ribbons. However, it is useful to introduce introduce a chirality parameter c following Schumer [7]. First we define a transfer efficiency t_E^i,

$$t_E^i = \frac{t_{ij}}{t_{ii} + t_{ij}} \ , \quad t_E^i \in [0;1] \ . \tag{5.2}$$

The transfer efficiency is large when the initial state i evolves into state j after encircling. Usint this we can define a chirality parameter c_i that compares the transfer efficiency for passing through the structure from the left t_E^i (going through the parameter circle counterclockwise) to passing through the structure in the opposite direction $t_E'^i$ (clockwise).

$$c_i = 4 \left(t_E^i - \frac{1}{2} \right) \left(t_E'^i - \frac{1}{2} \right) \ , \quad c_i \in [-1;1] \ . \tag{5.3}$$

The chirality parameter is positive when we find the same result irrespective of the direction in which we pass through the parameter circle, while a negative c_i indicates that the result depends on whether we go through the parameter circle clockwise or counterclockwise. In the quasi-adiabatic regime the chirality parameter is usually either minus one or one. Hence, for what we called 'chiral behavior' in Sec. 2.3 the chirality parameter evaluates to $c_i = -1$.

Using the chirality parameter c_i for the same ribbon as in Fig. 5.12, the information of eight lines in two plots can be condensed into one line (Fig. 5.16), repeating the statement of before, that for $r_{Re} > 0.09$ we observe chiral behavior. Using this compact representation we examine the chirality in the right panel of Fig. 5.16 in a larger range of r_{Re} and compare it to a longer ribbon. Although areas of non-chirality and chirality change, there remain large parameter ranges featuring chiral behavior.
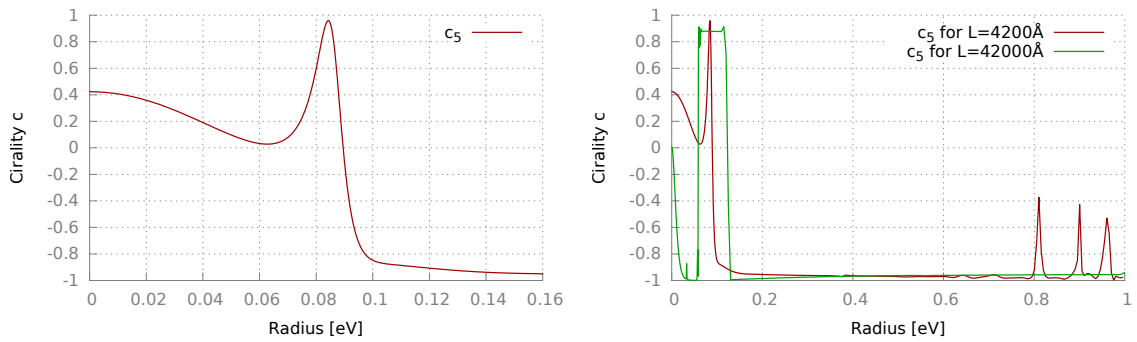
Figure 5.16: Chirality parameter c_5 giving the chirality for the fifth state according to Eq. (5.3). A value of minus one signifies that encircling in one direction yields the opposite result of encircling in the other direction. *Left panel:* Figure 5.12 summed up into the chirality parameter. The ribbon is $l = 4200$Å long. We find chiral behaviour for $r_{Re} > 0.09$. *Right panel:* Chirality for the same ribbon in a larger range of r_{Re} and in comparison with a longer ribbon $l = 42000$Å. The areas of chirality and non-chirality have changed, but (for a ribbon that is $4.2\mu m$ long!) there are large parameter ranges where we obtain chiral behavior.

5.4 Zigzag with sublattice splitting

In this section we discuss a generic EP in the V_z^0-Γ_z-plane for a $w = 85\text{Å}$ wide zigzag ribbon. The Riemann surface is shown in Fig 5.17 and the EPs are situated at $V_z^{\text{EP}} = 0.0 + i0.255$ and $V_z^{\text{EP}} = 0.0 - i0.255$, with a real crossing connecting them. The energy effectively is $E = 0.1$.
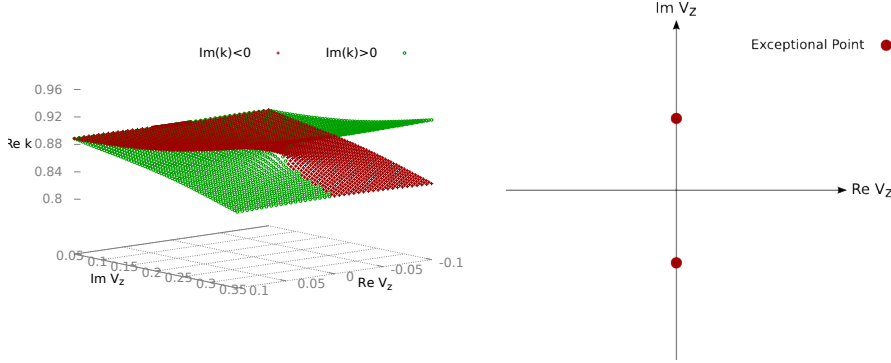

Figure 5.17: *Left panel:* Riemann surface for a $w = 85\text{Å}$ wide graphene nanoribbon. The sign of the imaginary part of the eigenvalue is color coded red (green) corresponds to gain (loss). *Right panel:* Position of the EPs in the complex parameter plane. The EPs are situated on the imaginary axis.

As described in section 5.2 we vary some parameters along the x-direction as shown in Fig. 5.18 on the left panel. This time the path in the $\text{Re}(V_z)$-$\text{Im}(V_z)$-plane is elliptical instead of circular. While we start on the $\text{Re}(V_z)$-axis for infinite waveguides, an elliptical path gives us more freedom to vary parameters, because a circular path can be realized for exactly one radius $r_{V_z} = \text{Im}(V_{z\text{EP}})$.

5.4.1 EP centered elliptical paths

In a first step we want to consider an elliptical path around the EP where we scan the semi-axis in the real direction r_{Re}. We start by considering only an oscillation in the real potential, with $r_{\text{Im}} = 0$. As displayed in Fig. 5.19, left panel, the transmission is one up until the potential is approximately larger than the energy of the electron. It is still able to tunnel quantum mechanically, as long as the potential is not too large. We find resonances at $r_{V_z} \approx 0.1417$ and $r_{V_z} \approx 0.142$.

The left panel in Fig. 5.19 introduces a small imaginary potential oscillation $r_{\text{Im}} = 0.001$. On one hand the resonances are shifted to slightly higher radii, on the other hand they are enhanced and exceed $T = 1$. For larger radii of r_{Im} the transmission stays $T = 1$ up to a higher r_{Re}, the resonances shift to higher values and new resonances appear. Note that this is far away from encircling the EP, but symmetric around the branch cut where the loss/gain behavior of the modes changes.

We find a consistent result in the reflection for the same device (see Fig. 5.20). Modes approaching from one side are absorbed and modes approaching from the other
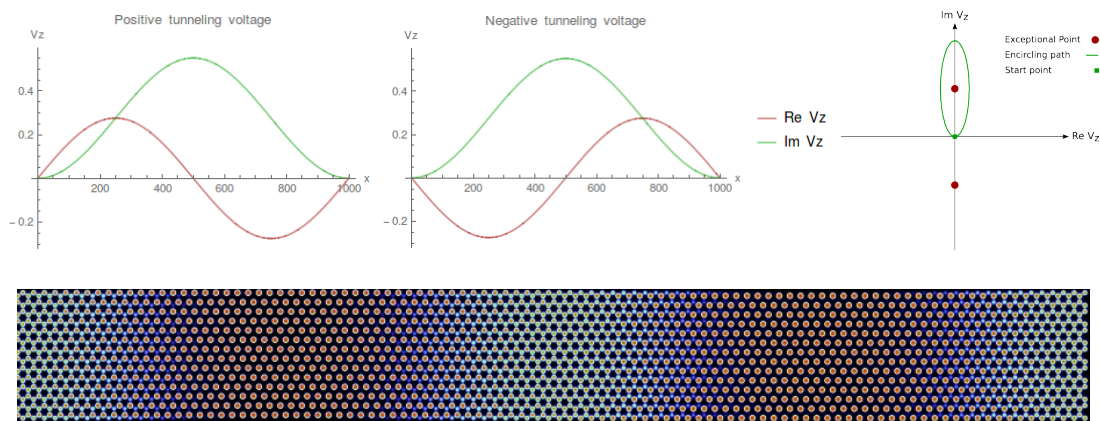
Figure 5.18: *Top panels:* Typical parameter variation in this chapter. The maximum in the imaginary potential will be prominent in the wavefunction plots (e.g. Fig. 5.24). *Lower panels:* Real part of the potential variation for shorter, narrower ribbon. There are parts where the two sublattices are approximately equal (bright) and where one sublattice is strongly favoured (dark). The color scale ranges from black (minimum) to red (maximum), same as in Fig. 5.14.

direction are reflected and amplified. The dips in the reflection are at the positions of the resonance-peaks in transmission[6]. The role of the left- and right-going modes is exchanged for reversed tunneling voltage (not shown). For very large radii the real potential dominates and the reflection approaches the $\mathrm{Im}(V_z) = 0$ limit, $R = R' = 1$ (also not shown).

Similarly as for the armchair ribbon in Sec. 5.2 we try to search for points fulfilling the conditions for unidirectional invisibility by comparing the reflections from both sides, the transmission and the transmission phase, see Fig. 5.21. At $r_{Re} = 0.1413$ all the conditions for unidirectional invisibility are fulfilled. We refer the reader to the discussion in Sec. 5.2. However, please note that this phenomenon is only valid at exactly this radius, distinguishing it from the unidirectional invisible Bragg gratings which have that feature over a certain frequency range.

---

[6]The reflection is not restricted by Lorentz reciprocity, which can be understood intuitively: depending on the incoming direction, the reflected wave mainly probes the region with dominantly loss/gain (compare with Fig. 5.18).
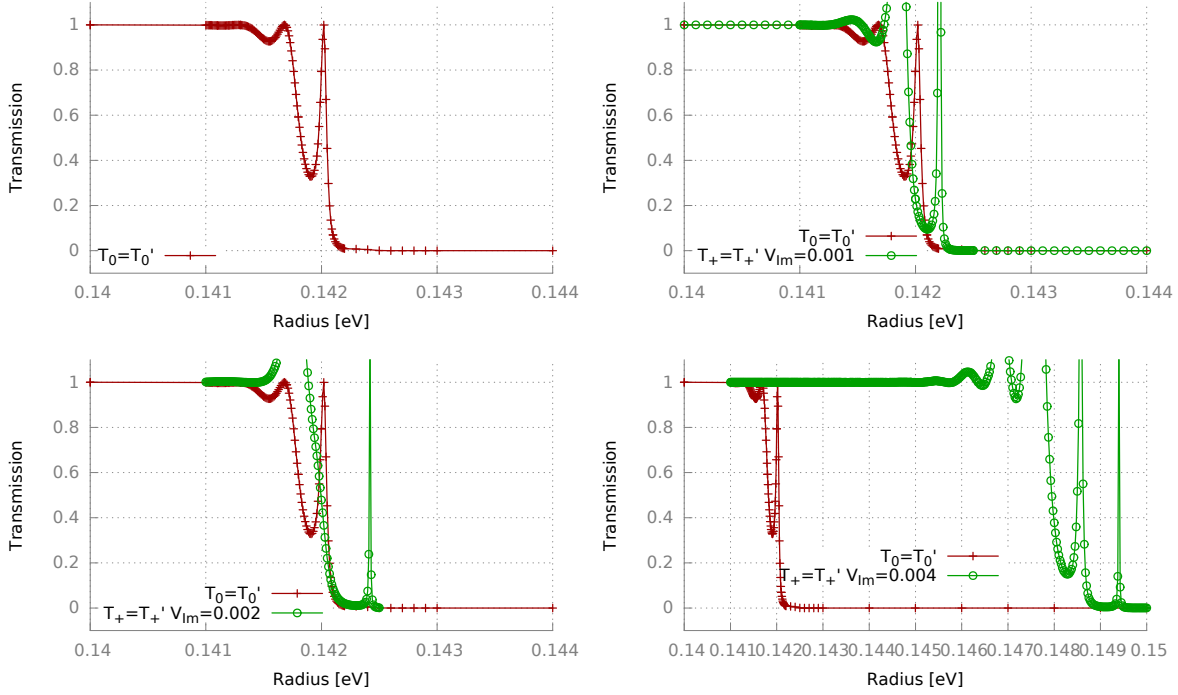
Figure 5.19: Transmission as a function of the real radius r_{Re} with the center fixed at the EP. The ribbon is $w = 85$Å wide and $l = 2400$Å. We study the effect of an increasing imaginary amplitude. *Upper left panel:* No imaginary potential. There are two resonances present. *Upper right panel:* Imaginary potential amplitude $V_{Im} = 0.001$, the peaks have shifted slightly to higher radii and are amplified. *Lower left panel:* Imaginary potential amplitude $V_{Im} = 0.002$, the peaks shift to even higher radii. *Lower right panel:* Imaginary potential amplitude $V_{Im} = 0.004$. Apparently the movement is not linear as the peaks are shifted to much higher radii. Furthermore, three new peaks have appeared.
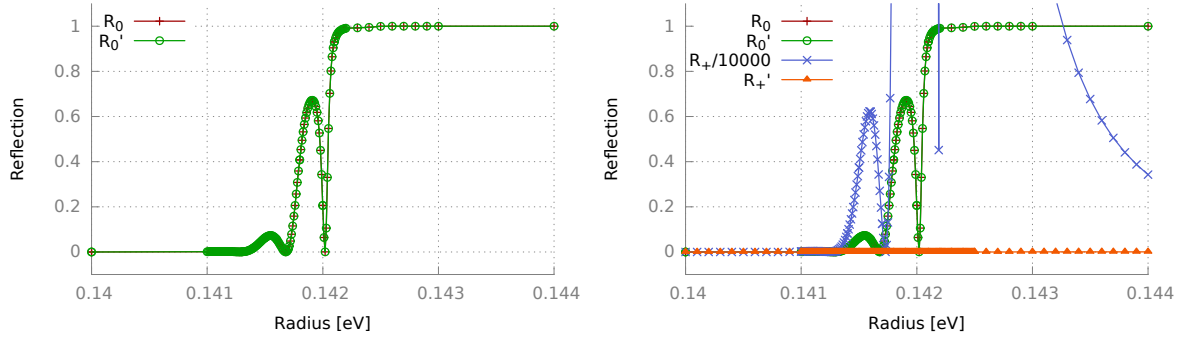
Figure 5.20: Reflection for the same ribbon as in Fig. 5.19. *Left panel:* Reflection without an imaginary potential. The dips are at the same position as the peaks in the transmission, agreeing with $T_0 + R_0 = 1$. *Right panel:* Reflection with an oscillation of the imaginary potential with amplitude $r_{im} = 0.001$. The positions of the dips still agree with the positions of the peaks, although reflection in one direction is strongly damped while it is strongly amplified in the other.
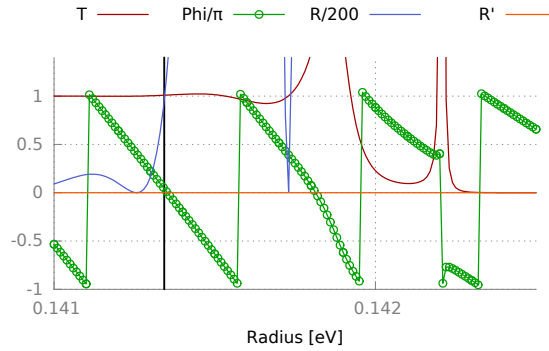
Figure 5.21: Transmission, transmission phase and reflectivities in both directions for an ellipse with a complex semi-axis of $r_{Im} = 0.001$ and variable r_{Re} (same as the upper right panel in Fig. 5.19). The vertical black line at $r_{Re} = 0.1413$ marks the point where the phase shift due to the potential vanishes, the transmission is equal to one and the reflectivity is enhanced in one and damped in the other direction. Hence, we have unidirectional invisibility at that point.

5.4.2 Elliptical paths with variable center

As in the previous section, we hope to gain insight by moving the center of the ellipse along the real axis. When the ellipse is centered around the EP (zero on the x-axis), transmission is one. Moving the center of the ellipse for fixed $r_{Re} = 0.1$, $r_{Im} = 0.275$ along the real axis, we find maximal transmission at $V_{zcenter} \approx 0.018$ (compare with Fig. 5.22). At first glance, the change in transmission arises due to the competition between the real and imaginary potential. However, this does not explain why the point of maximum transmission is shifted to $V_{zcenter} \approx 0.018$. We can gain some insight by comparing with the Riemann surface Fig. 5.17, whose color-coding shows the gain-loss structure. If the ellipse is centered around the EP, the amount of gain and loss which the state undergoes is equal, so the transmission at $V_{zcenter} = 0$ is one. If the ellipse is shifted slightly to one side, gain or loss takes over. The interplay between the gain-loss structure and the real potential results in a maximum at $V_{zcenter} \approx 0.18$.
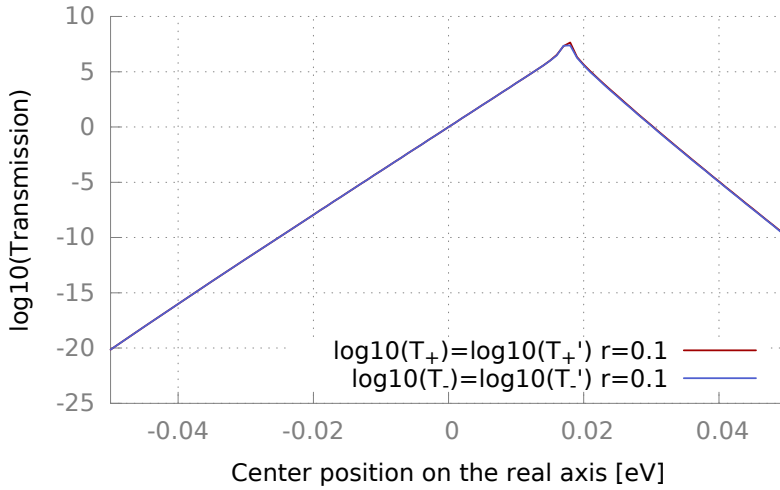

Figure 5.22: Transmission of a $w = 85\text{Å}$ wide and $l = 2400\text{Å}$ long nanoribbon for which the sublattice splitting potential V_z runs through an ellipse in the complex plane. The imaginary radius and center are chosen as $\text{Im}V_{zcenter} = 0.275$ and $r_{im} = 0.275$ such that the ellipse for $\text{Re}V_{zcenter} = 0$ is centered around the EP. For an EP-centered ellipse the transmission is one, for $\text{Re}V_{zcenter} < 0$ it drops and for $\text{Re}V_{zcenter} < 0$ it grows with a maximum at $\text{Re}V_{zcenter} \approx 0.018$.

Strikingly, for most of parameter circles the reflectivities are approximately the same for both directions, $R \approx R'$. This is in contrast to previous results, where the potential was odd w.r.t. the center of the ribbon. The imaginary potential is symmetric around the center of the ribbon (see Fig. 5.18), therefore reflection in both directions is equal, as long as the reflected wave does not probe the area around the branch cut. The symmetric imaginary potential is also visible in the absolute square of the wavefunction $|\psi|^2$ (see Fig. 5.24). At points of suppressed ($V_{zcenter} = -0.018$), approximately perfect ($V_{zcenter} = 0.0$) and enhanced ($V_{zcenter} = 0.018$) transmission shows that the imaginary potential (which is fixed) produces an area of strong gain in the center of the ribbon.
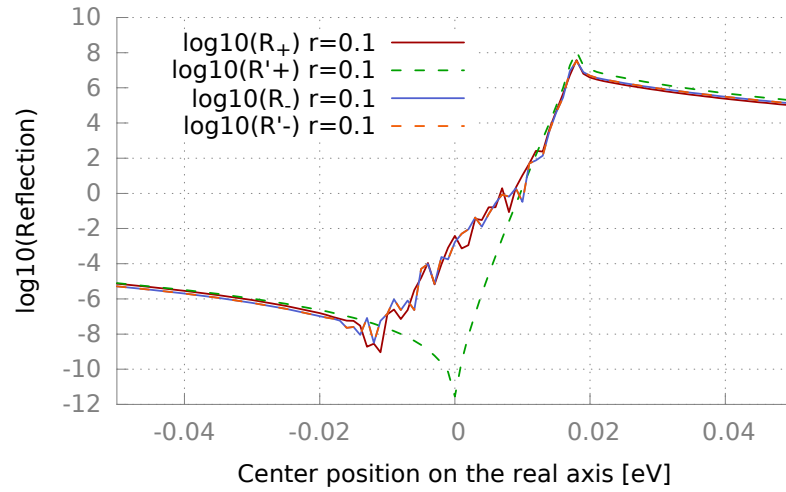
Figure 5.23: Reflection for the same ribbon as in 5.22. Note that the reflection is approximately equal in both directions $R = R'$.
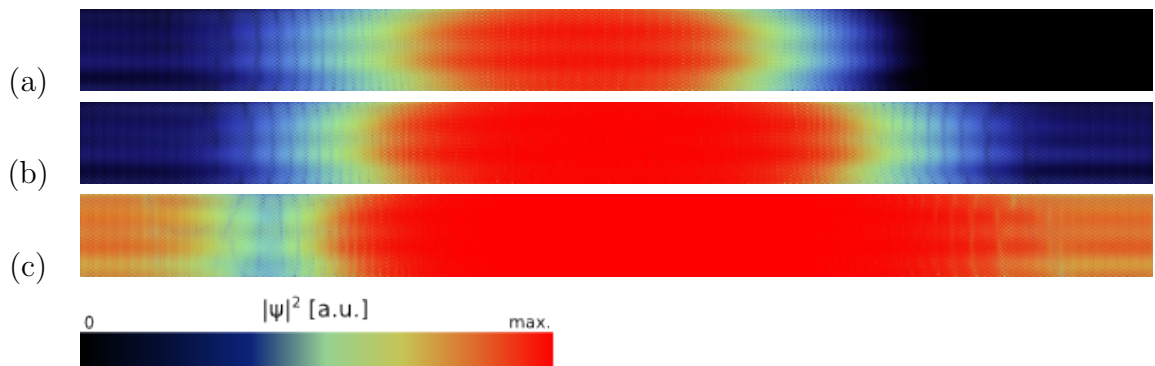
Figure 5.24: Absolute square of the wavefunction $|\psi|^2$ for the same ribbon as in Fig. 5.22 at *(a)* $V_{zcenter} = -0.018$, *(b)* $V_{zcenter} = 0.0$ and *(c)* $V_{zcenter} = 0.018$. The color scale is logarithmic, otherwise the area with gain in the center of the ribbon would oversaturate. The imaginary potential is fixed and gives an area of strong gain in the center of the ribbon. The variable transmission arises due to the competition between the real and imaginary potential.

6 Conclusion and Outlook

We conclude with an overview of the topics covered in this thesis and highlight the conclusions that were drawn. We also present a few thoughts concerning future research and realization in experiment.

In the course of this masters thesis we investigated the existence, location and dynamics in the presence of exceptional points in graphene nanoribbons. Chapters 2 and 3 introduced the necessary background and proved the existence of exceptional points in bulk graphene, consistent with the literature about hexagonal optical lattices [10]. The subsequent chapter (Chap. 4) explored the dependence of the k-eigenvalues as a function of various external potentials. We were able to identify two kinds of exceptional points in graphene nanoribbons, which we called generic and non-generic EPs. The former occurs for every state that has a gap, irrespective of the type of ribbon, the latter emerges only at real crossings in the inverse bandstructure of armchair ribbons. Actually, all borders of bandgaps are generic EPs, because there is a transition from real k to imaginary k (compare with Fig. 4.8).

We determined that generic EPs can be probed as a function of external parameters by varying on-site potentials or hopping parameters. By tracking the movement of the generic EP when slowly tuning away from balanced gain and loss we found that there is no EP in the absence of at least one sublattice with gain (or loss, respectively). Non-generic EPs appear for a complex grating potential (compare with Fig. 4.2) and form around real crossings. However, the nature of these crossings and the magnitude of the imaginary part of the complex modes surrounding them depends strongly on the width of the ribbon. Because they do not occur at the same (or easily predictable) energy in every ribbon we named them non-generic EPs.

With several EPs identified we subsequently investigated the dynamics in their vicinity. In the introduction we referred to the dynamical encircling of an EP by Doppler et al. [3] as an inspiration for this thesis. It turns out, that the dynamics around generic EPs are limited by the principle of Lorentz reciprocity, which relates incoming and outgoing currents. The states that form the generic EP propagate in opposite directions, leading to the fact that there is only one mode contributing to transport through the nanoribbon. Without breaking Lorentz reciprocity the total transmission (i.e. transmission through that single mode) has to be equal in both directions. Hence, the asymmetric switch presented by Doppler et al. cannot be transferred to the dynamical encircling of a generic EP in graphene nanoribbons. For a non-generic EP, however, the two modes that are connected propagate into the same direction. In this case it is possible to 'convert' one mode into the other $t_{ij} \neq t_{ji}$ and have different mode to mode transmissions

in both scattering directions $t_{ij} \neq t'_{ij}$, while preserving[1] $T = T'$. In Sec. 5.3 we show that encircling a non-generic EP yields chiral behavior, i.e. the outgoing state depends on the encircling direction of the EP.

For generic EPs we could identify a certain parameter-variation which is impossible to detect from one direction. The phenomenon is described in the literature as 'unidirectional invisibility' [46, 47, 48]. An experiment that probes this particular potential from one direction will find no reflection, a transmission equal to one and no phase shift in the transmitted mode. Probing the structure in the other direction, an enhanced reflection will be found.

There are, of course, certain limitations to the findings in this thesis, which perhaps legitimate future research.

Although using a complex potential is an effective treating of the surroundings, the underlying interactions are assumed to be fully coherent. This requires perfect alignment of the graphene flakes to enable momentum conserving tunneling which takes a lot of effort to realize in an experiment [49, 50]. While is possible to create systems with coherent loss it is very hard to implement coherent gain. However, the findings in Sec. 4.3.4 suggest that it is necessary to have gain somewhere in the system. This is certainly not conclusive, and different potentials, materials or exceptional points can be investigated to eliminate the necessity of coherent gain.

Concerning the experiment we want to stress that this thesis presented principles, and was not restricted to realistic parameter combinations. In the course of planning an experiment, a more extensive discussion of possible substrates and the resulting (complex) local potentials will be necessary. This will require detailed calculations based on realistic parameters either from experiment or from ab-inition parametrizations. A realistic simulation will also have to incorporate that the nanoribbons in an experiment will have imperfect edges and defects, which might have drastic effects, especially on non-generic EPs.

Although graphene has been investigated extensively both experimentally, and theoretically, more detailed studies of the behavior of complex modes, similar to Fig. 4.12, potentially can provide even further insight into the nature of this fascinating material and the complexity of bandstructures themselves. Perhaps there are ways to extract new information from a bandstructure in the four-dimensional space spanned by $\mathrm{Re}E$, $\mathrm{Im}E$, $\mathrm{Re}k$ and $\mathrm{Im}k$.

Summing up, this thesis was able to find exceptional points and phenomena associated with them in graphene. It was able to extend the current state of the literature concerning exceptional points in graphene nanoribbons and made general contributions towards the realization of an experiment demonstrating exceptional point physics in graphene nanoribbons.

---

[1] $T = \sum_{ij} t_{ij}$

7 Acknowledgements

At the end of this thesis I want to thank the people who made this work possible and contributed to it.

First and foremost I want to express my gratitude to my advisor Assistant Prof. Florian Libisch. His inspiring lectures motivated me to start working in this field and with his thorough understanding of physics he led me to many insights over the past two years. In countless occasions he helped me to resolve the problems that inevitably arise when writing a Diploma thesis. Thank you, Florian, for all the time and patience you invested in me.

I am also very grateful for the discussions with Alexander Schumer and Prof. Stefan Rotter, who shared their deep insight into non-hermitian and exceptonal point physics with us. They helped me understand EP physics.

In many weekly meetings Valerie Smejkal, Thomas Fabian, Lukas Linhardt and Eduardo Schiavo asked the right questions to test my ideas, found errors and pointed me to the right direction.

Special thanks for the great time I was allowed to spend at the Institute of Theoretical Physics are due to all my colleagues, please excuse me, but you are just too many to mention at this place. However, I want to point out the warm welcome I received by the Theoretical Quantum Dynamics group, led by Prof. Joachim Burgdörfer.

And at last, but certainly not least, I am sincerely grateful for the support of my parents and family throughout this thesis and, even more, my studies. Without their moral and financial support this would not have been possible. For their complementary role, I want to thank my flatmates and friends, who worked very hard to occasionally distract me from physics. A special mention is undoubtedly due to my girlfriend, Johanna Hütner, for her patience with me and her corrections and comments to this thesis.

In the end I want to apologize to everyone whom I forgot to mention here.

Bibliography

[1] Nimrod Moiseyev. *Non-hermitian quantum mechanics*, volume 9780521889. Cambridge University Press, Cambridge, 2011.

[2] W D Heiss. The physics of exceptional points. *Journal of Physics A: Mathematical and Theoretical*, 45(44):444016, nov 2012.

[3] Jörg Doppler, Alexei A. Mailybaev, Julian Böhm, Ulrich Kuhl, Adrian Girschik, Florian Libisch, Thomas J. Milburn, Peter Rabl, Nimrod Moiseyev, and Stefan Rotter. Dynamically encircling an exceptional point for asymmetric mode switching. *Nature*, 537(7618):76–79, sep 2016.

[4] M. Born and V. Fock. Beweis des Adiabatensatzes. *Zeitschrift für Physik*, 51(3-4):165–180, mar 1928.

[5] K S Novoselov, A K Geim, S V Morozov, D Jiang, Y Zhang, S V Dubonos, I V Grigorieva, and A A Firsov. Electric field effect in atomically thin carbon films. *Science*, 306(5696):666–669, oct 2004.

[6] John R. Schaibley, Hongyi Yu, Genevieve Clark, Pasqual Rivera, Jason S. Ross, Kyle L. Seyler, Wang Yao, and Xiaodong Xu. Valleytronics in 2D materials, 2016.

[7] Alexander Schumer. Non-Hermitian dynamics in the vicinity of an exceptional point, 2017.

[8] Maurizio Fagotti, Claudio Bonati, Demetrio Logoteta, Paolo Marconcini, and Massimo MacUcci. Armchair graphene nanoribbons: PT-symmetry breaking and exceptional points without dissipation. *Physical Review B - Condensed Matter and Materials Physics*, 83(24), 2011.

[9] Alexander Szameit, Mikael C Rechtsman, Omri Bahat-Treidel, and Mordechai Segev. PT-symmetry in honeycomb photonic lattices. *Physical Review A - Atomic, Molecular, and Optical Physics*, 84(2), 2011.

[10] Bo Zhen, Chia Wei Hsu, Yuichi Igarashi, Ling Lu, Ido Kaminer, Adi Pick, Song Liang Chua, John D. Joannopoulos, and Marin Soljačić. Spawning rings of exceptional points out of Dirac cones - Supplementary Information. *Nature*, 525(7569):354–358, sep 2015.

[11] G. Gamov. Zur Quantentheorie des Atomkerns. *Zeitschrift f\"ur Physik*, 51(3-4):204–212, mar 1928.

Bibliography

[12] Ramy El-Ganainy, Konstantinos G. Makris, Mercedeh Khajavikhan, Ziad H. Musslimani, Stefan Rotter, and Demetrios N. Christodoulides. Non-Hermitian physics and PT symmetry. *Nature Physics*, 14(1):11–19, jan 2018.

[13] W. D. Heiss and W. H. Steeb. Avoided level crossings and Riemann sheet structure. *Journal of Mathematical Physics*, 32(11):3003–3007, nov 1991.

[14] W. D. Heiss. Repulsion of resonance states and exceptional points. *Physical Review E - Statistical Physics, Plasmas, Fluids, and Related Interdisciplinary Topics*, 61(1):929–932, jan 2000.

[15] Klaus Petermann. Calculated Spontaneous Emission Factor for Double-Heterostructure Injection Lasers with Gain-Induced Waveguiding. *IEEE Journal of Quantum Electronics*, 15(7):566–570, jul 1979.

[16] Hamidreza Ramezani, Tsampikos Kottos, Vassilios Kovanis, and Demetrios N Christodoulides. Exceptional-point dynamics in photonic honeycomb lattices with PT symmetry. *Physical Review A - Atomic, Molecular, and Optical Physics*, 85(1), 2012.

[17] Soo Young Lee, Jung Wan Ryu, Jeong Bo Shim, Sang Bum Lee, Sang Wook Kim, and Kyungwon An. Divergent Petermann factor of interacting resonances in a stadium-shaped microcavity. *Physical Review A - Atomic, Molecular, and Optical Physics*, 78(1), 2008.

[18] W.D. Heiss. Phases of wave functions and level repulsion. *The European Physical Journal D - Atomic, Molecular and Optical Physics*, 7(1):1–4, aug 1999.

[19] Raam Uzdin, Alexei Mailybaev, and Nimrod Moiseyev. On the observability and asymmetry of adiabatic state flips generated by exceptional points. *Journal of Physics A: Mathematical and Theoretical*, 44(43):435302, oct 2011.

[20] S. N. Ghosh and Y. D. Chong. Exceptional points and asymmetric mode conversion in quasi-guided dual-mode optical waveguides. *Scientific Reports*, 6(1):19837, apr 2016.

[21] Ido Gilary, Alexei A. Mailybaev, and Nimrod Moiseyev. Time-asymmetric quantum-state-exchange mechanism. *Physical Review A - Atomic, Molecular, and Optical Physics*, 88(1):010102, jul 2013.

[22] M V Berry and R Uzdin. Slow non-Hermitian cycling: Exact solutions and the Stokes phenomenon. *Journal of Physics A: Mathematical and Theoretical*, 44(43):435303, oct 2011.

[23] Thomas J. Milburn, Jörg Doppler, Catherine A. Holmes, Stefano Portolan, Stefan Rotter, and Peter Rabl. General description of quasiadiabatic dynamical phenomena near exceptional points. *Physical Review A - Atomic, Molecular, and Optical Physics*, 92(5):052124, nov 2015.

[24] H. Xu, D. Mason, Luyao Jiang, and J. G.E. Harris. Topological energy transfer in an optomechanical system with exceptional points. *Nature*, 537(7618):80–83, sep 2016.

[25] Absar U. Hassan, Gisela L. Galmiche, Gal Harari, Patrick Likamwa, Mercedeh Khajavikhan, Mordechai Segev, and Demetrios N. Christodoulides. Chiral state conversion without encircling an exceptional point. *Physical Review A*, 96(5), 2017.

[26] M. V. Berry. Quantal Phase Factors Accompanying Adiabatic Changes. *Proceedings of the Royal Society A: Mathematical, Physical and Engineering Sciences*, 392(1802):45–57, mar 1984.

[27] Alexei A. Mailybaev, Oleg N. Kirillov, and Alexander P. Seyranian. Geometric phase around exceptional points. *Physical Review A - Atomic, Molecular, and Optical Physics*, 72(1):014104, jul 2005.

[28] Luca Banszerus, Michael Schmitz, Stephan Engels, Jan Dauber, Martin Oellers, Federica Haupt, Kenji Watanabe, Takashi Taniguchi, Bernd Beschoten, and Christoph Stampfer. Ultrahigh-mobility graphene devices from chemical vapor deposition on reusable copper. *Science Advances*, 1(6):e1500222–e1500222, jul 2015.

[29] Jinming Cai, Pascal Ruffieux, Rached Jaafar, Marco Bieri, Thomas Braun, Stephan Blankenburg, Matthias Muoth, Ari P. Seitsonen, Moussa Saleh, Xinliang Feng, Klaus Müllen, and Roman Fasel. Atomically precise bottom-up fabrication of graphene nanoribbons. *Nature*, 466(7305):470–473, jul 2010.

[30] P. R. Wallace. The band theory of graphite. *Physical Review*, 71(9):622–634, may 1947.

[31] A H Castro Neto, F Guinea, Nuno M R Peres, Kostya S Novoselov, and Andre K Geim. The electronic properties of graphene. *Reviews of modern physics*, 81(1):109, 2009.

[32] M. I. Katsnelson, K. S. Novoselov, and A. K. Geim. Chiral tunnelling and the Klein paradox in graphene. *Nature Physics*, 2(9):620–625, sep 2006.

[33] F. Libisch, S. Rotter, J. Güttinger, C. Stampfer, and J. Burgdörfer. Transition to Landau levels in graphene quantum dots. *Physical Review B*, 81(24):245411, jun 2010.

[34] Nikolai A. Poklonski, Eugene F. Kislyakov, Sergey A. Vyrko, Oleg N. Bubel', and Sergey V. Ratkevich. Electronic band structure and magnetic states of zigzag graphene nanoribbons: quantum chemical calculations. *Journal of Nanophotonics*, 6(1):061712, oct 2012.

[35] Young Woo Son, Marvin L Cohen, and Steven G Louie. Energy gaps in graphene nanoribbons. *Physical Review Letters*, 97(21), 2006.

[36] Li Yang, Cheol Hwan Park, Young Woo Son, Marvin L. Cohen, and Steven G. Louie. Quasiparticle energies and band gaps in graphene nanoribbons. *Physical Review Letters*, 99(18), 2007.

[37] Wen-Xiao Wang, Mei Zhou, Xinqi Li, Si-Yu Li, Xiaosong Wu, Wenhui Duan, and Lin He. Energy gaps of atomically precise armchair graphene nanoribbons. *arXiv*, 2016.

[38] B Sachs, T O Wehling, M I Katsnelson, and A I Lichtenstein. Adhesion and electronic structure of graphene on hexagonal boron nitride substrates. *Physical Review B*, 84(19):195414, 2011.

[39] Nils M Freitag, Tobias Reisch, Larisa A Chizhova, Peter Nemes-Incze, Christian Holl, Colin R Woods, Roman V Gorbachev, Yang Cao, Andre K Geim, Kostya S Novoselov, Joachim Burgdörfer, Florian Libisch, and Markus Morgenstern. Tunable giant valley splitting in edge-free graphene quantum dots on boron nitride. *Nature Nanotechnology*, 2017.

[40] Flemming Besenbacher, Erik Lægsgaard, and Ivan Stensgaard. Fast-scanning STM studies. *Materials Today*, 8(5):26–30, may 2005.

[41] Tony Low and F Guinea. Strain-induced pseudomagnetic field for novel graphene electronics. *Nano Letters*, 10(9):3551–3554, 2010.

[42] F. Guinea, A. K. Geim, M. I. Katsnelson, and K. S. Novoselov. Generating quantizing pseudomagnetic fields by bending graphene ribbons. *Physical Review B - Condensed Matter and Materials Physics*, 81(3):1–5, 2010.

[43] J. von Neumann and E. P. Wigner. Über merkwürdige diskrete Eigenwerte. *Physikalische Zeitschrift*, 30:465, 1929.

[44] Florian Libisch. *Electronic structure and transport in mesoscopic devices*. PhD thesis, TU Wien, 2009.

[45] Dirk Jalas, Alexander Petrov, Manfred Eich, Wolfgang Freude, Shanhui Fan, Zongfu Yu, Roel Baets, Miloš Popović, Andrea Melloni, John D. Joannopoulos, Mathias Vanwolleghem, Christopher R. Doerr, and Hagen Renner. What is-and what is not-an optical isolator. *Nature Photonics*, 7(8):579–582, 2013.

[46] Zin Lin, Hamidreza Ramezani, Toni Eichelkraut, Tsampikos Kottos, Hui Cao, and Demetrios N. Christodoulides. Unidirectional invisibility induced by PT-symmetric periodic structures. *Physical Review Letters*, 106(21):213901, may 2011.

[47] Alois Regensburger, Christoph Bersch, Mohammad Ali Miri, Georgy Onishchukov, Demetrios N. Christodoulides, and Ulf Peschel. Parity-time synthetic photonic lattices. *Nature*, 488(7410):167–171, aug 2012.

[48] Liang Feng, Ye Long Xu, William S. Fegadolli, Ming Hui Lu, José E.B. Oliveira, Vilson R. Almeida, Yan Feng Chen, and Axel Scherer. Experimental demonstration of a unidirectional reflectionless parity-time metamaterial at optical frequencies. *Nature Materials*, 12(2):108–113, feb 2013.

[49] Shujie Tang, Haomin Wang, Yu Zhang, Ang Li, Hong Xie, Xiaoyu Liu, Lianqing Liu, Tianxin Li, Fuqiang Huang, Xiaoming Xie, and Mianheng Jiang. Precisely aligned graphene grown on hexagonal boron nitride by catalyst free chemical vapor deposition. *Scientific Reports*, 3(1):2666, dec 2013.

[50] A. Mishchenko, J. S. Tu, Y. Cao, R. V. Gorbachev, J. R. Wallbank, M. T. Greenaway, V. E. Morozov, S. V. Morozov, M. J. Zhu, S. L. Wong, F. Withers, C. R. Woods, Y. J. Kim, K. Watanabe, T. Taniguchi, E. E. Vdovin, O. Makarovsky, T. M. Fromhold, V. I. Fal'ko, A. K. Geim, L. Eaves, and K. S. Novoselov. Twist-controlled resonant tunnelling in graphene/boron nitride/graphene heterostructures. *Nature Nanotechnology*, 9(10):808–813, oct 2014.